

Multivariate Time Series Data Imputation via Distributionally Robust Regularization

Che-Yi Liao^{1*}, Zheng Dong², Gian-Gabriel Garcia³, Kamran Paynabar¹

¹Georgia Institute of Technology, Atlanta, GA, USA

²Amazon.com, Inc., Seattle, WA, USA

³University of Washington, Seattle, WA, USA

Abstract

Multivariate time series (MTS) imputation is often compromised by mismatch between observed and true data distributions—a bias exacerbated by non-stationarity and systematic missingness. Standard methods that minimize reconstruction error or encourage distributional alignment risk overfitting these biased observations. We propose the Distributionally Robust Regularized Imputer Objective (DRIO), which jointly minimizes reconstruction error and the divergence between the imputer and a worst-case distribution within a Wasserstein ambiguity set. We derive a tractable dual formulation that reduces infinite-dimensional optimization over measures to adversarial search over sample trajectories, and propose an adversarial learning algorithm compatible with flexible deep learning backbones. Comprehensive experiments on diverse real-world datasets show DRIO consistently improves imputation under both missing-completely-at-random and missing-not-at-random settings, reaching Pareto-optimal trade-offs between reconstruction accuracy and distributional alignment.

1 Introduction

Multivariate time series (MTS) data are ubiquitous across scientific and engineering domains, arising naturally in applications such as traffic monitoring, healthcare operations, industrial sensor networks, and environmental surveillance [Ghosh et al., 2009, Kirchgässner et al., 2012, Hamilton, 2020, Liao et al., 2022, 2025b, Hsiao et al., 2025, Yang et al., 2025, Liao et al., 2025c]. These data encode rich spatiotemporal dependencies that are critical for downstream tasks including forecasting, anomaly detection, and decision-making. However, real-world time series measurements are frequently incomplete due to sensor failures, communication dropouts, or resource constraints, which highlights the importance of robust imputation methods to recover missing entries before subsequent analysis and decision-making [Li et al., 2020, Emmanuel et al., 2021, Zhang et al., 2025, Liao et al., 2025a, Cai et al., 2025].

In this MTS imputation task, the primary challenge is the **mismatch between the true data-generating process and the observed empirical distribution**. In other words, the observed data distribution $\hat{\mathbb{P}}_N$ can be a biased estimator of the true data-generation distribution \mathbb{P}_{true} , causing classical imputation methods to fail as they fit to the observed entries. This bias stems from two intertwined factors: (a) time series data non-stationarity and (b) systematic missing pattern.

*Contact Information: cliao48@gatech.edu

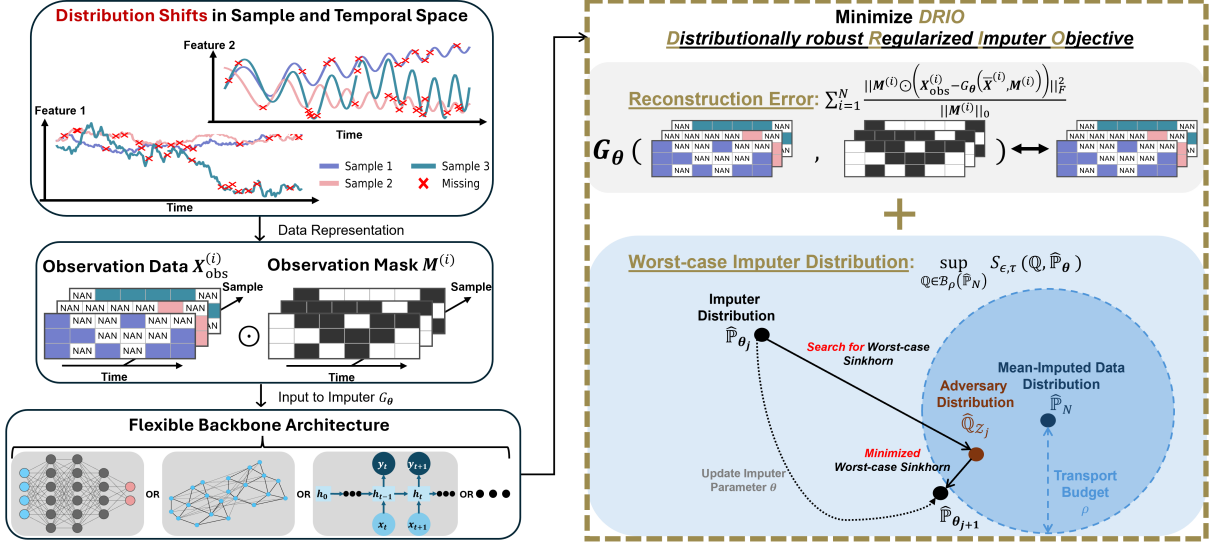


Figure 1: Overview of Multivariate Time Series Imputation under DRIO.

First, *time series data non-stationarity* is a common phenomenon wherein the underlying data-generating process evolves over either temporal or sample space [Sayed-Mouchaweh and Lughofer, 2012, Cheng et al., 2015, Ditzler et al., 2015]. For example, in traffic modeling, weekday and weekend traffic patterns may exhibit markedly different statistical dependencies while different sensor locations can show distinct traffic flow patterns. Consequently, reliable estimation of the data distribution becomes progressively more challenging as the feature-temporal dimensionality increases and the non-stationary dynamics grow more complex [Dixit and Jain, 2023, Tran et al., 2019].

This distribution estimation complexity can further be exaggerated by *non-uniform missingness pattern* across MTS data entries. While measurements may be missing completely at random (MCAR) with each entry has an identical and independent probability of being unobserved, missing not at random (MNAR) are particularly prevalent in practice [Bollinger et al., 2014, Pham et al., 2022, Cai et al., 2025]. Under MNAR, the probability of missingness depends on the underlying features and their values and time. This systematic selection bias causes specific regions of the data manifold to remain unobserved, introducing another layer of complexity in learning from incomplete time series.

While numerous time series imputation methods have been developed, they rarely *explicitly* address this mismatch between empirical distribution and true data-generating process. Existing methods typically assume that minimizing reconstruction error on observed entries or the divergence between imputers and the empirical distributions will generalize to missing entries and other samples Zhang et al. [2025], Afrifa-Yamoah et al. [2020], Cao et al. [2018], Shen et al. [2023], Mattei and Frellsen [2019], Ipsen et al. [2020], Muzellec et al. [2020]. However, these methods can fail when empirical distribution is a biased sample of the true data manifold since they do not directly incorporate *bias* or *uncertainty* of distributional alignment into imputation.

To mitigate this distributional uncertainty around empirical distribution of observed data entries, we propose a novel **Distributionally robust Regularized Imputer Objective** (DRIO), which enables the model to hedge its predictions against worst-case distributional alignment within a Wasserstein

ambiguity set centered at the empirical measures (Figure 1). DRIO acts as a regularizer that controls the trade-off between point-wise reconstruction accuracy and robustness of the imputer by minimizing the risk against an adversarial distribution that exploits the support bias of the observed data. DRIO is designed to be compatible with any deep imputer model backbone architecture, which enables various architectures to maintain their unique design advantages while enhancing their robustness to potentially biased data.

Contribution. Our main contributions are summarized as follows:

- (i) We are among the first to **formalize the non-stationary MTS imputation under distribution shifts** by explicitly addressing the distributional mismatch between observed data and the true data-generating process.
- (ii) We propose a novel distributionally robust regularizer (DRIO) that **balances reconstruction accuracy and worst-case distributional shifts**. Moreover, we **derive a tractable dual formulation** (Theorem 3.2) that reduces the infinite-dimensional optimization over measures to an adversarial search over samples.
- (iii) We **develop an efficient alternating optimization algorithm** (Algorithm 1) that jointly updates adversarial trajectories and imputer parameters, enabling end-to-end training with flexible deep learning backbones.
- (iv) We provide extensive empirical evidence across 10 diverse real-world datasets showing that **DRIO achieves robust imputation performance under both MCAR and MNAR mechanisms at varying missing ratios** (10%/50%/90%), reaching Pareto frontier between reconstruction accuracy and distributional alignment.

2 Related Work

MTS imputation methods can be broadly categorized by their learning objectives into *point-wise* reconstruction and *distributional* alignment.

Spatiotemporal Architectures and Point-wise Methods. Early deep learning approaches primarily utilized Recurrent Neural Networks (RNNs) to capture temporal dependencies. For instance, Cao et al. [2018] proposed a bidirectional recurrent system (BRITS) that treats missing values as latent variables within a recurrent graph, while other works have explored multi-directional attention [Suo et al., 2020] and error-tolerant systems for real-time applications [Ma et al., 2020]. To address spatial correlations in networked systems such as traffic sensors, Spatio-Temporal Graph Neural Networks (ST-GNNs) and convolutional architectures were introduced [Li et al., 2020, Shen et al., 2023]. Specifically, Ye et al. [2021] combined graph attention with temporal convolutions (GACN), and Marasca et al. [2022] developed a sparse spatiotemporal attention mechanism (SPIN) to propagate information across sparse observations without relying on potentially biased intermediate imputations. Despite their architectural sophistication, these methods typically minimize L_2 reconstruction error on observed entries. This point-wise focus often causes models to overfit the empirical distribution of the training set, failing to generalize when the underlying generating process evolves.

Distributional Alignment and Generative Models. To address the limitations of point-estimates, recent research has pivoted to generative models that estimate the conditional distribution of missing data. Adversarial models like GAIN [Yoon et al., 2018] use a hint-vector discriminator

to enforce realistic samples, while diffusion-based approaches such as CSDI [Tashiro et al., 2021] and DiffImp [Gao et al., 2024] leverage score-based modeling for high-quality probabilistic samples. Within the Variational Autoencoder framework, MIWAE [Mattei and Frellsen, 2019] and not-MIWAE [Ipsen et al., 2020] were designed to handle missing-not-at-random (MNAR) data via importance weighting. Notably, SCVAE [Li et al., 2021] introduced a shift correction mechanism to handle concentrated missingness; however, it requires exact domain knowledge to pre-specify the missing pattern, limiting its utility in agnostic non-stationary settings where dynamics evolve unpredictably.

A significant advancement in this domain involves the application of Optimal Transport (OT) to enforce geometric alignment between imputed and observed distributions [Muzellec et al., 2020, Huang et al., 2025]. For example, the Proximal Spectrum Wasserstein (PSW) framework [Wang et al., 2025a] extends OT to the frequency domain to handle non-stationary periodicities. While these methods can account for temporal dynamics, they fundamentally assume the observed empirical distribution is an unbiased proxy for the true distribution. They therefore remain vulnerable to systematic selection biases, such as MNAR mechanisms, which truncate the true data manifold as observations. In contrast, our proposed DRIO framework does not treat the empirical measure as an absolute reference; instead, it hedges against distributional uncertainty by regularizing the imputer against a worst-case distribution within a Wasserstein ambiguity set, ensuring robustness to the biased correlations inherent in non-stationary observations.

3 Method

3.1 Preliminaries

Background and Notation. We denote \mathbb{P}_{true} as the probability distribution underlying the data-generating process that describes joint evolution of D correlated features (e.g., sensors, spatial nodes) over time. We assume this process is observed at discrete timestamps $t \in \{1, \dots, T\}$ and a single realization forms a ground truth trajectory $\mathbf{X} \in \mathbb{R}^{D \times T}$. Since \mathbb{P}_{true} captures complex time-varying dependencies on the feature-temporal space, the marginal distributions of features may shift significantly over the temporal horizon.

With the definition of data-generating process, we denote $\{\mathbf{X}^{(1)}, \dots, \mathbf{X}^{(N)}\} \in \mathbb{R}^{N \times D \times T}$ as N trajectories drawn from \mathbb{P}_{true} . To account for missing entries, we define an observation mask as $\mathbf{M}^{(i)} \in \{0, 1\}^{D \times T}$, which is a realization from a random matrix such that $\mathbf{M}_{d,t}^{(i)} = 1$ if $\mathbf{X}_{d,t}^{(i)}$ is observed and 0 otherwise. Consequently, the i^{th} sample trajectory is denoted by $\mathbf{X}_{\text{obs}}^{(i)} := \mathbf{X}^{(i)} \odot \mathbf{M}^{(i)}$, where \odot is the Hadamard product (See top left of Figure 1). Moreover, we define the empirical mean value for feature d at a time t as $\bar{x}_{d,t} := \sum_i \mathbf{X}_{\text{obs},d,t}^{(i)} / \sum_j \mathbf{M}_{d,t}^{(j)}$. We set $\bar{x}_{d,t} = 0$ if $\sum_j \mathbf{M}_{d,t}^{(j)} = 0$. Consequently, the i^{th} mean-imputed sample is defined as $\bar{\mathbf{X}}^{(i)}$ where $\bar{\mathbf{X}}_{d,t}^{(i)} := \mathbf{X}_{\text{obs},d,t}^{(i)} + (1 - \mathbf{M}_{d,t}^{(i)}) \bar{x}_{d,t}$. Moreover, $\widehat{\mathbf{X}}^{(i)} := \mathbf{X}_{\text{obs}}^{(i)} + (1 - \mathbf{M}^{(i)}) G_{\boldsymbol{\theta}}(\mathbf{X}_{\text{obs}}^{(i)}, \mathbf{M}^{(i)})$ is the imputed data by imputer $G_{\boldsymbol{\theta}}$ parametrized by $\boldsymbol{\theta}$.

Sinkhorn Divergence. Let $\mu, \nu \in \mathcal{P}(\mathbb{R}^{D \times T})$ be two probability measures, where $\mathcal{P}(S)$ denotes the collection of all distributions supported on space S . The entropic unbalanced transport cost is defined as $W_{\epsilon,\tau}(\mu, \nu) := \inf_{\pi \geq 0} \left\{ \int \|\mathbf{x} - \mathbf{z}\|_F^2 d\pi + \epsilon \text{KL}(\pi \mid \mu \otimes \nu) + \tau(\text{KL}(\pi_1 \mid \mu) + \text{KL}(\pi_2 \mid \nu)) \right\}$, where π is a positive measure with marginals π_1 and π_2 , $\epsilon > 0$ controls entropic regularization, and $\tau > 0$ governs marginal relaxation that allows mass creation and destruction. The Unbalanced Sinkhorn Divergence is then: $S_{\epsilon,\tau}(\mu, \nu) := W_{\epsilon,\tau}(\mu, \nu) - \frac{1}{2}(W_{\epsilon,\tau}(\mu, \mu) + W_{\epsilon,\tau}(\nu, \nu))$.

While Wasserstein- p distance is a natural choice for measuring distributional discrepancy, its exact computation requires solving a linear program that yields a non-smooth objective. Therefore, it is common to adopt the Sinkhorn Divergence since the entropic regularization enables efficient GPU-parallelizable computation and produces a fully differentiable objective, while the debiasing formula further corrects the entropic bias, ensuring that $S_{\epsilon,\tau}(\mu, \mu) = 0$ Muzellec et al. [2020], Wang et al. [2025a]. Moreover, Sinkhorn Divergence provides meaningful gradients even when distribution supports are disjoint, which is a robust alternative compared to other likelihood-based metrics, e.g., KL divergence, and point-wise metrics, e.g., least-square [Villani et al., 2008, Séjourné et al., 2019, Wang et al., 2025b]. Notably, the *Unbalanced* Sinkhorn Divergence relaxes the strict mass conservation of standard optimal transport, allowing local mass creation and destruction via a soft penalty [Séjourné et al., 2019]. This prevents outliers from dominating gradient updates (whether this outlier is from the ambiguity set or from poorly performing imputer predictions), thereby ensuring training stability. We expand the discussions of our design choices in Appendix §A.

3.2 Distributionally Robust Imputation Regularizer

Our robust imputation objective (DROI) jointly minimizes *point-wise reconstruction accuracy* of the observed data and *worst-case divergence* of the empirical distribution to its neighbors. In this section, we first detail the worst-case divergence problem, then provide the primal view of the proposed robust imputation objective.

Ambiguity Set Construction. Since raw data has missing entries, we construct a Wasserstein ambiguity set centered at the empirical distribution of the *mean-imputed data* (Bottom right of Figure 1). Conceptually, this set contains all distributions that could plausibly have generated the observed data, with the set radius (transport budget) controlling the degree of distributional uncertainty and thus the robustness level. Specifically, we define the *empirical measure* as $\widehat{\mathbb{P}}_N := \sum_i \delta_{\bar{\mathbf{X}}^{(i)}}/N$ and the *ground cost* as $c_{\mathbf{X}}(\mathbf{Z}) = \|\mathbf{X} - \mathbf{Z}\|_F^2$, where $\mathbf{X}, \mathbf{Z} \in \mathbb{R}^{D \times T}$. The ambiguity set $\mathcal{B}_\rho(\widehat{\mathbb{P}}_N)$ is then defined as the set of all probability measures \mathbb{Q} supported on a subset of $\mathbb{R}^{D \times T}$ satisfying a transport budget constraint:

$$\mathcal{B}_\rho(\widehat{\mathbb{P}}_N) := \left\{ \mathbb{Q} \in \mathcal{P}(\mathbb{R}^{D \times T}) : \inf_{\pi \in \Pi(\widehat{\mathbb{P}}_N, \mathbb{Q})} \mathbb{E}_{(\mathbf{X}, \mathbf{Z}) \sim \pi} [c_{\mathbf{X}}(\mathbf{Z})] \leq \rho \right\}, \quad (1)$$

where $\Pi(\widehat{\mathbb{P}}_N, \mathbb{Q})$ denotes the set of couplings between the empirical and candidate distributions, and $\rho \geq 0$ is the radius of the uncertainty set representing the transport budget.

Remark 3.1 (Ambiguity Set Geometry). We construct our ambiguity set (1) using the Wasserstein metric centered on the empirical measure of the mean-imputed data for practical considerations specific to our imputation problem. First, centering the ambiguity set at the empirical distribution of the mean-imputed data $\{\bar{\mathbf{X}}^{(i)}\}$ allows exploration of the missing entries starting from the mean, subject to the transport budget ρ . Moreover, the empirical measure $\widehat{\mathbb{P}}_N$ is a discrete collection of point masses from the mean-imputed data, which are realizations from a potentially continuous ground-truth distribution \mathbb{P}_{true} . With the Wasserstein ambiguity set definition, we explicitly accommodate continuity in the support of the learned worst-case distribution, effectively creating a continuous neighborhood around the empirical distribution. Finally, this formulation enables the imputer to learn the correlation structure of the distribution without being constrained by summary statistics (e.g., moments) that may be biased estimates of the ground truth. \square

Primal Objective. With the ambiguity set underlying the observed data, we now formulate the primal DROI objective, which jointly minimizes (i) the reconstruction error of the imputer,

and (ii) the distributional alignment between the worst-case data distribution and the imputer-generated distribution *over ambiguity set*. To measure distributional discrepancy, we adopt the *Unbalanced Sinkhorn Divergence*, a differentiable approximation of Wasserstein-2 distance that relaxes mass-matching constraints.

We define $\widehat{\mathbb{P}}_{\theta}$ as the empirical distribution induced by applying the imputer G_{θ} to the observed dataset, i.e., $\widehat{\mathbb{P}}_{\theta} := \sum_{i=1}^N \delta_{\widehat{\mathbf{X}}^{(i)}}/N$, where $\widehat{\mathbf{X}}^{(i)}$ is the i^{th} imputed sample. Then, our imputation objective is minimizing the combination of reconstruction error and the worst-case Unbalanced Sinkhorn Divergence between the imputer distribution and candidate distributions \mathbb{Q} within the ambiguity set. Accordingly, we define our primal objective as:

$$\min_{\theta} \alpha R_{\theta} + (1 - \alpha) \sup_{\mathbb{Q} \in \mathcal{B}_{\rho}(\widehat{\mathbb{P}}_N)} S_{\epsilon, \tau}(\mathbb{Q}, \widehat{\mathbb{P}}_{\theta}), \quad (2)$$

where $R_{\theta} := \sum_{i=1}^N \|\mathbf{M}^{(i)} \odot (\mathbf{X}^{(i)} - \widehat{\mathbf{X}}^{(i)})\|_F^2 / \|\mathbf{M}^{(i)}\|_0$ represents the reconstruction error normalized by the number of observed entries. Here, $\|\cdot\|_0$ denotes the matrix zero-norm (counting non-zero elements), and $\alpha \in [0, 1]$ is the trade-off between point-wise fidelity and the distributional robustness of the imputer. By simultaneously minimizing the reconstruction error on observed data and the worst-case divergence between the imputer distribution $\widehat{\mathbb{P}}_{\theta}$ and the adversarial \mathbb{Q} , the imputer prevents overfitting to the biased empirical distribution from the observed data while maintaining the ability to impute the data point-wise. **Dual Formulation of Imputation Objective.** Solving (2) is computationally intractable because it involves a supremum over an infinite-dimensional space of probability measures \mathbb{Q} . Now, we demonstrate that solving it can be reduced to solving a tractable dual representation, a minimax problem over *deterministic adversarial sample trajectories*.

Theorem 3.2 (Tractable Relaxation of Robust Imputation). *Let $\mathcal{Z} = \{\zeta^{(i)}\}_{i=1}^N \in \mathbb{R}^{N \times D \times T}$ be the batch of adversarial trajectories. Define $\widehat{\mathbb{Q}}_{\mathcal{Z}} := \frac{1}{N} \sum_{i=1}^N \delta_{\zeta^{(i)}}$ as the empirical adversary distribution. Then, the worst-case distributional alignment, i.e.,*

$$\sup_{\mathbb{Q} \in \mathcal{B}_{\rho}(\widehat{\mathbb{P}}_N)} S_{\epsilon, \tau}(\mathbb{Q}, \widehat{\mathbb{P}}_{\theta}), \quad (3)$$

is upper-bounded by

$$\inf_{\gamma \geq 0} \left\{ \gamma \rho + \sup_{\mathcal{Z} \in \mathbb{R}^{N \times D \times T}} \left(S_{\epsilon, \tau}(\widehat{\mathbb{Q}}_{\mathcal{Z}}, \widehat{\mathbb{P}}_{\theta}) - \gamma C_{\mathcal{Z}} \right) \right\}, \quad (4)$$

where $C_{\mathcal{Z}} := \sum_{i=1}^N c_{\widehat{\mathbf{X}}^{(i)}}(\zeta^{(i)})/N$.

Proof Sketch. We first relax the hard constraint on the ambiguity set radius ρ by introducing a Lagrange multiplier γ . Since the Unbalanced Sinkhorn loss is convex with respect to the input measure, the inner maximization involves optimizing a convex functional over a convex set. Consequently, the supremum is achieved at an extreme point of the feasible set, which implies that the worst-case distribution collapses to a discrete empirical measure supported on a deterministic adversarial batch \mathcal{Z} . This result effectively reduces the intractable search over infinite-dimensional probability measures \mathbb{Q} to a tractable search over the finite-dimensional tensor \mathcal{Z} . The full proof is provided in Appendix §B. \square

Theorem 3.2 establishes that maximizing over probability measures \mathbb{Q} reduces to finding the adversary that maximizes the divergence between its empirical measure $\widehat{\mathbb{Q}}_{\mathcal{Z}}$ and the imputer distribution

$\widehat{\mathbb{P}}_{\boldsymbol{\theta}}$, subject to a penalty on over-exploration. Due to the convexity of the Unbalanced Sinkhorn Divergence over measure space, strong duality may not hold. However, this formulation remains theoretically sufficient and practically effective for two reasons. First, the dual objective serves as a *surrogate upper bound* on the worst-case risk. Therefore, if the model is robust against this dual upper bound, it is by definition robust against the primal worst-case scenario. Second, the true transport budget ρ is an unknown property of the data-generating process and in practice will be tuned by cross-validation along with the multiplier γ , resulting in optimized performance based on validation results.

3.3 Practical Implementation of DRIO

While Theorem 3.2 provides a mathematically tractable formulation for the worst-case divergence term in our primal objective (2), solving for the optimal Lagrange multiplier γ that strictly satisfies a specific budget ρ remains computationally challenging because it involves updating $\boldsymbol{\theta}$ (imputer), γ (dual variable), and \mathcal{Z} (adversary) iteratively.

Final DRIO Objective. To alleviate this computational burden, we observe that for any $\rho > 0$, there exists a unique $\gamma \geq 0$ that yields the *same optimal solution* to (4). Consequently, we can treat γ as a fixed hyperparameter and remove the dependency on ρ . That is, with a fixed γ , DRIO is defined as:

$$\min_{\boldsymbol{\theta}} \alpha R_{\boldsymbol{\theta}} + (1 - \alpha) \sup_{\mathcal{Z}} (S_{\epsilon, \tau}(\widehat{\mathbb{Q}}_{\mathcal{Z}}, \widehat{\mathbb{P}}_{\boldsymbol{\theta}}) - \gamma C_{\mathcal{Z}}). \quad (\text{DRIO})$$

In this form, α controls the trade-off between reconstruction error and worst-case distributional alignment and γ effectively controls the level of robustness. Larger γ increases penalty on the adversary's transport cost, limiting the worst-case distribution to remain close to the empirical data. Conversely, smaller γ allows exploring a broader neighborhood of the empirical distribution for imputation.

Training Imputer with DRIO. We develop an alternating learning procedure (Algorithm 1) to solve (DRIO) via two update in each iteration. First, we fix the model parameters $\boldsymbol{\theta}$ and update the adversarial batch \mathcal{Z} to identify the worst-case distributional shift centered at the observations. Then, we update the imputer parameters $\boldsymbol{\theta}$ to minimize the reconstruction error and the worst-case divergence. We detail these steps below.

Step 1: Inner Maximization (Adversary Update). In this step, we fix the imputer parameters $\boldsymbol{\theta}$ and search for the worst-case adversarial batch. Each adversary is initialized at the global mean of the observations, i.e., $\zeta_{d,t}^{(i)} = \bar{x}_{d,t}$ for all samples i in the training batch. Then, we update these adversaries by gradient ascent to increase the Sinkhorn divergence $S_{\epsilon, \tau}$, while simultaneously restricting it to the observed data via the ground cost penalty $\gamma C_{\mathcal{Z}}$. To ensure computational efficiency and stability, we fix the imputed data (thus $\widehat{\mathbb{P}}_{\boldsymbol{\theta}}$) and detach it from the computation graph to prevent updates to $\boldsymbol{\theta}$ during this step.

Step 2: Outer Minimization (Imputer Update). In the second step, we fix the discovered adversarial batch and update the imputer parameters $\boldsymbol{\theta}$ by gradient descent to minimize our imputation objective (DRIO), with fixed adversaries. The imputer thus learns to reconstruct the observations while forcing the generated trajectories to cover the support of the worst-case data manifold defined by the transport budget and the observed samples.

Cross-Validation. Hyperparameter tuning for imputation is challenging since ground truth missing values are unavailable at deployment. Unlike methods that create artificial masks for self-supervised validation [Tashiro et al., 2021], we train the imputer to reconstruct observed entries in the training

Algorithm 1 Training MTS Imputer with DRIO

```

1: Input: Dataset  $\mathcal{D}$ , trade-off  $\alpha$ , robustness  $\gamma$ , inner steps  $K$ , batch size  $B$ , learning rates  $\eta_\zeta, \eta_\theta$ 
2: Initialize: Imputer parameters  $\boldsymbol{\theta}$  randomly
3: for each batch  $\{\mathbf{X}_{\text{obs}}^{(i)}, \mathbf{M}^{(i)}\}_{i=1}^B \sim \mathcal{D}$  do
4:   Compute batch mean:  $\bar{\mathbf{X}}_{d,t} \leftarrow \sum_i^B \mathbf{X}_{\text{obs},d,t}^{(i)} / \sum_j \mathbf{M}_{d,t}^{(j)}$ 
5:   Generate imputation:  $\widehat{\mathbf{X}}^{(i)} \leftarrow \mathbf{X}_{\text{obs}}^{(i)} + (\mathbf{1} - \mathbf{M}^{(i)}) \odot G_{\boldsymbol{\theta}}(\mathbf{X}_{\text{obs}}^{(i)}, \mathbf{M}^{(i)})$ 
6:   Initialize adversary:  $\mathcal{Z}_0 \leftarrow \{\zeta^{(i)} : \zeta_{d,t}^{(i)} = \bar{x}_{d,t}\}_{i=1}^B$ 
7:   // Inner maximization
8:   for  $k = 1$  to  $K$  do
9:      $J(\mathcal{Z}_{k-1}) \leftarrow S_{\epsilon,\tau}(\widehat{\mathbb{Q}}_{\mathcal{Z}_{k-1}}, \widehat{\mathbb{P}}_{\boldsymbol{\theta}}) - \frac{\gamma}{B} \sum_{i=1}^B c_{\bar{\mathbf{X}}}(\zeta_{k-1}^{(i)})$ 
10:     $\mathcal{Z}_k \leftarrow \mathcal{Z}_{k-1} + \eta_\zeta \nabla_{\mathcal{Z}} J(\mathcal{Z}_{k-1})$ 
11:   end for
12:   // Outer minimization
13:   Re-generate imputation:  $\widehat{\mathbf{X}}^{(i)} \leftarrow \mathbf{X}_{\text{obs}}^{(i)} + (\mathbf{1} - \mathbf{M}^{(i)}) \odot G_{\boldsymbol{\theta}}(\mathbf{X}_{\text{obs}}^{(i)}, \mathbf{M}^{(i)})$ 
14:   Compute loss:  $\mathcal{L}(\boldsymbol{\theta}) \leftarrow \alpha R_{\boldsymbol{\theta}} + (1 - \alpha) S_{\epsilon,\tau}(\widehat{\mathbb{Q}}_{\mathcal{Z}_K}, \widehat{\mathbb{P}}_{\boldsymbol{\theta}})$ 
15:   Update:  $\boldsymbol{\theta} \leftarrow \boldsymbol{\theta} - \eta_\theta \nabla_{\boldsymbol{\theta}} \mathcal{L}(\boldsymbol{\theta})$ 
16: end for

```

set and validate on reconstruction error of *observed entries* on a held-out validation set. This strategy is fully deployable and allows the model to learn within-sample dependencies from entire (un)observed entries that generalizes to *unseen samples*. The optimal (α, γ) is selected by minimizing validation MSE. Details and comparative analysis are provided in Appendix C.3 and §4, respectively.

Imputer Model Backbone. (DRIO) is model-agnostic. The imputer $G_{\boldsymbol{\theta}}$ takes two inputs: the partially observed data $\mathbf{X}_{\text{obs}}^{(i)} \in \mathbb{R}^{D \times T}$, where missing entries are initialized via batch-wise mean imputation $\bar{\mathbf{X}}^{(i)}$, and the binary observation mask $\mathbf{M}^{(i)} \in \{0, 1\}^{D \times T}$. These are concatenated along the channel dimension to form an input tensor of shape $\mathbb{R}^{B \times 2 \times D \times T}$, and the imputer outputs a deterministic reconstruction $\widehat{\mathbf{X}}^{(i)} \in \mathbb{R}^{D \times T}$. This flexibility allows seamless integration with various architectures with special design advantages. We evaluate various model backbones in our ablation studies (§4).

4 Numerical Experiments

We conduct comprehensive experiments to answer three questions: **(a)** How does the proposed objective (DRIO) perform across diverse datasets and missing mechanisms? **(b)** What are the benefits of our design choices? **(c)** How effective is our reconstruction-based cross-validation strategy? Due to space constraints, detailed experimental settings and extended performance comparison results with sensitivity analyses are provided in Appendix C. Code is available at: <https://anonymous.4open.science/r/DRIO-DD40>.

Datasets. We evaluate on ten commonly used publicly available MTS datasets spanning healthcare, manufacturing, transportation, and environmental monitoring (Table 1), with sample sizes $N \in [165, 4000]$, features $D \in [3, 82]$, and sequence lengths $T \in [24, 207]$, providing a comprehensive benchmark for assessing imputation performance on distinct real-data scenarios. To evaluate imputers' performances, we introduce artificial missingness for each dataset then partition them into train/validation/test splits (70/10/20%). All splits are normalized using entry-wise mean and

standard deviation from the training set to ensure fair comparison and prevent leakage.

Table 1: Dataset summary. All datasets are presented as (N, D, T) tensors representing samples \times features \times time steps.

Dataset	N	D	T	Description
CNNpred	165	78	60	Quarters (5 US indices combined) \times market indicators \times trading days
PEMS08	170	3	62	Sensors \times (flow, occupancy, speed) \times days
PM2.5	260	7	168	Weeks \times meteorological features \times hours
GasSensor	290	16	150	Experiment chunks (58 exp \times 5 chunks) \times sensors \times time steps (2.5Hz, 60s per chunk)
Gait	300	6	101	Gait cycles (10 subjects \times 3 conditions \times 10 reps) \times joint angles \times phase (%)
PEMS04	307	3	59	Sensors \times (flow, occupancy, speed) \times days
CMAPSS	359	21	207	Engines (with ≥ 207 cycles from four engines) \times sensor measurements \times cycles
AirQuality	389	13	24	Days \times environmental features \times hours
HAR	2947	9	128	Activity windows \times signals \times time steps
PhysioNet	4000	35	48	ICU patients \times clinical variables \times hours

Missing Data Mechanisms. We consider both MCAR and MNAR scenarios with missing ratios of 10%, 50%, and 90%, applied on observed entries. For MCAR, we uniformly mask a fraction of entries independent of their values. For MNAR, we simulate a realistic pattern where extreme values are more likely to be missing [Bollinger et al., 2014, Pham et al., 2022]. Specifically, each entry $\mathbf{X}_{d,t}^{(i)}$ is assigned a missing probability proportional to $\Phi(|z_{d,t}^{(i)}|)$, where $z_{d,t}^{(i)} = (\mathbf{X}_{d,t}^{(i)} - \bar{\mathbf{x}}_d)/\sigma_d$ is the z-score computed from *feature-wise* mean ($\bar{\mathbf{x}}_d$) and standard deviation (σ_d) over the entire dataset, and Φ is the standard normal CDF. This ensures values farther from the mean have higher missingness probability.

Benchmarks. We compare against two baselines and five state-of-the-art methods. For baselines, **Mean** imputes with the sample mean per (feature, time) position, i.e., $\bar{\mathbf{x}}_{d,t}$; **MF** (Matrix Factorization) performs low-rank completion by flattening temporal and feature dimensions. For state-of-the-art deep learning methods, **BRITS** [Cao et al., 2018] is a bidirectional recurrent neural network that learns missing values through recurrent dynamics, combining reconstruction loss with consistency constraints between forward and backward predictions. **CSDI** [Tashiro et al., 2021] uses conditional score-based diffusion models, treating observed values as conditioning information to generate imputations through iterative denoising. **notMIWAE** [Ipsen et al., 2020] extends variational autoencoders to handle MNAR by modeling the missingness mechanism jointly with the data distribution. For OT methods, **MDOT** [Muzellec et al., 2020] minimizes Wasserstein distance for matrix completion (we flatten temporal-feature dimensions), and **PSW** [Wang et al., 2025a] uses proximal Sinkhorn distances for single time series (applied per sample).

Unless otherwise specified, DRIO is paired with the BRITS backbone and selected $\alpha \in \{0.01, 0.25, 0.5, 0.75, 0.99\}$ and $\gamma \in \{0.1, 1.0, 5.0, 10.0\}$ according to our reconstruction-based cross-validation procedure described in §3 and Appendix C.3. We train all deep learning methods with maximum 30 epochs and iterative methods (MF, MDOT) with maximum 1000 iterations.

Metrics. We employ two complementary metrics capturing point-wise reconstruction accuracy and distributional alignment on the test set. First, we evaluate reconstruction error using mean-square error (**MSE**) strictly on *artificially masked unobserved entries* where ground truth is available. Let

Table 2: MSE and W2 under MNAR missing mechanism, averaged across missing ratios. **Bold** indicates top 3 performance per dataset. nMW is short for notMIWAE. DRIO is paired with BRITS backbone architecture. Full results with standard deviation is presented at Table 6 in Appendix C.6.2.

Dataset	Baselines		Benchmarks				Ours		
	Mean	MF	CSDI	MDOT	PSW	BRITS	nMW	DRIO	
<i>MSE (Imputation Accuracy)</i>									
CNNpred	1.35	1.67	1.31	0.98	1.31	0.76	2.24	0.74	
PEMS08	1.20	2.37	49.76	0.65	0.38	0.54	2.83	0.52	
PM2.5	1.49	1.76	1.07	1.17	0.42	0.91	3.00	0.63	
GasSensor	1.40	0.57	0.64	0.41	0.02	0.08	1.28	0.09	
Gait	0.33	0.85	0.07	0.18	0.30	0.21	2.47	0.15	
PEMS04	0.81	1.55	0.24	0.41	0.38	0.43	2.68	0.41	
CMAPSS	1.15	1.16	0.14	0.79	0.93	0.36	0.65	0.27	
AirQuality	0.92	1.73	0.21	0.54	0.41	0.35	2.34	0.32	
HAR	1.23	1.90	0.29	0.77	0.42	0.46	2.16	0.33	
PhysioNet	1.35	2.26	0.75	1.13	0.72	0.87	7.83	0.79	
<i>W2 (Distributional Alignment)</i>									
CNNpred	0.33	0.20	0.40	0.29	0.19	0.36	0.71	0.32	
PEMS08	0.31	0.46	2.53	0.25	0.09	0.32	0.89	0.29	
PM2.5	0.46	0.36	0.41	0.42	0.23	0.44	0.83	0.39	
GasSensor	0.44	0.15	0.35	0.28	0.02	0.10	0.57	0.06	
Gait	0.12	0.16	0.08	0.09	0.15	0.17	0.80	0.11	
PEMS04	0.28	0.34	0.18	0.22	0.10	0.25	0.89	0.23	
CMAPSS	0.40	0.22	0.10	0.28	0.21	0.24	0.39	0.21	
AirQuality	0.30	0.28	0.16	0.25	0.14	0.27	0.79	0.21	
HAR	0.46	0.13	0.17	0.33	0.15	0.32	0.65	0.26	
PhysioNet	0.45	0.23	0.26	0.41	0.21	0.36	1.47	0.33	

$\Delta^{(i)} := \mathbf{X}^{(i)} - \widehat{\mathbf{X}}^{(i)}$ denote the residual between ground truth $\mathbf{X}^{(i)}$ and imputation $\widehat{\mathbf{X}}^{(i)}$ for sample i . Then,

$$\text{MSE} := \frac{\sum_{i \in \mathcal{D}} \|\overline{\mathbf{M}}_{\text{gt}}^{(i)} \odot \Delta^{(i)}\|_F^2}{\sum_{j \in \mathcal{D}} \|\overline{\mathbf{M}}_{\text{gt}}^{(j)}\|_0}, \quad (5)$$

where \mathcal{D} is the evaluation set, $\overline{\mathbf{M}}_{\text{gt}}^{(i)}$ is a binary matrix with 1 indicating missing entry for sample i , and $\|\cdot\|_0$ counts non-zero elements. We further evaluate distributional alignment using Wasserstein-2 (**W2**) for *missing values*. We aggregate all imputed values (and ground truths) at missing entries across samples, features, and time steps into one-dimensional empirical distributions and compute the closed-form 1D Wasserstein-2 distance (See Appendix C.4 for the formula).

4.1 Results

To answer the questions in §4, we present results by imputation performance, ablation studies, and validation strategy analysis.

Imputation Performance. Table 2 presents imputation results under the MNAR mechanism, where extreme values have higher missingness probability. For MSE, DRIO remains the only method to achieve top-3 performance across all 10 datasets, demonstrating its robustness to systematic selection bias. Notably, DRIO attains the lowest MSE on CNNpred (0.74), Gait (0.15), CMAPSS (0.27), and AirQuality (0.32). Compared to the MCAR setting (Table 5 in Appendix C.6), DRIO

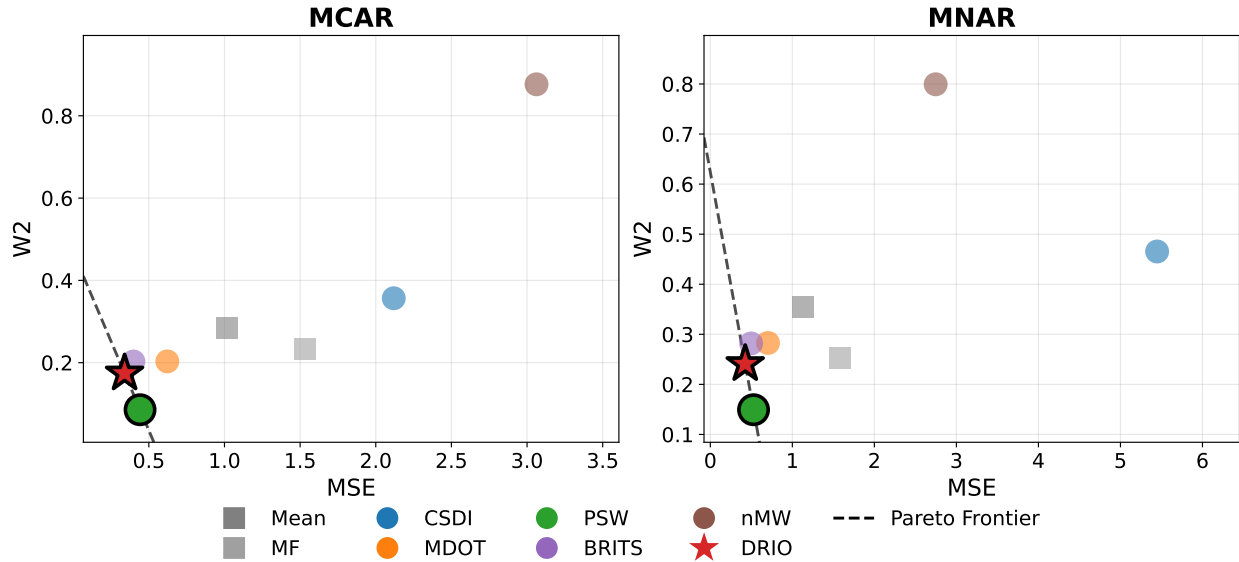


Figure 2: Trade-off Between MSE and W2 averaged across all datasets and missing ratios under MCAR (left) and MNAR (right). DRIO and PSW lie at the Pareto front at both cases, with DRIO offering lower MSE at comparable W2.

exhibits mild performance degradation, whereas other methods show more pronounced sensitivity to the missing mechanism. CSDI continues to struggle with non-stationary traffic data, with MSE on PEMS08 escalating from 14.11 under MCAR to 49.76 under MNAR, indicating that diffusion-based approaches are particularly vulnerable when missingness correlates with data values. Notably, notMIWAE (nMW) performs poorly across all datasets, likely because its effectiveness depends on correct specification of the missingness mechanism, which is unknown in practice. For W2, we first note that DRIO minimizes *worst-case* Sinkhorn divergence over an ambiguity set rather than sample Wasserstein distance. Therefore, it hedges against distribution shift at the cost of not always achieving minimum W2. That said, DRIO achieves top-3 performance on 7 of 10 datasets, with PSW generally attaining the lowest values due to its direct optimization of Wasserstein distance. These results confirm that DRIO’s distributionally robust regularization provides effective hedging against the compounded challenges of non-stationarity and systematic missingness inherent in real-world MNAR settings.

Next, we visualize the trade-off between MSE and W2 in Figure 2 by averaging across datasets and missing ratios. Notably, both DRIO and PSW lie on the Pareto frontier, meaning no method dominates them on both metrics. Specifically, DRIO achieves a favorable balance with lower MSE and competitive W2, confirming that DRIO effectively balances reconstruction accuracy and distributional alignment.

Ablation Study. Comparing *Backbone Architecture*, Table 3 shows that under the DRIO objective, BRITS achieves the best performance, followed by Long Short-Term Memory (LSTM), confirming that bidirectional temporal modeling is critical for MTS imputation. Attention-based architectures, including Graph Attention (GAT) and Spatio-temporal transformer (STT) exhibit substantially higher error and variance, suggesting self-attention struggles to capture sequential dependencies without extensive tuning. These results demonstrate the importance of model backbone and motivate

Table 3: Ablation study on training objectives and model backbone architectures. Mean (standard deviation) of MSE and W2 across datasets and missing ratios. **Bold** indicates best performer. BSH-DRIO represents DRIO with balanced Sinkhorn divergence.

Objective	Arch.	MCAR		MNAR	
		MSE	W2	MSE	W2
DRIO	MLP	0.74(0.52)	0.22(0.20)	0.83(0.58)	0.27(0.23)
	LSTM	0.66(0.57)	0.19(0.18)	0.74(0.63)	0.24(0.21)
	GAT	1.61(3.40)	0.35(0.64)	1.60(3.05)	0.36(0.56)
	STT	1.93(3.33)	0.41(0.70)	1.35(1.00)	0.32(0.28)
	BRITS	0.33(0.23)	0.18(0.18)	0.44(0.31)	0.24(0.21)
BSH-DRIO	BRITS	0.59(0.33)	0.31(0.28)	0.71(0.43)	0.35(0.30)
MSE	BRITS	0.34(0.24)	0.19(0.19)	0.45(0.32)	0.25(0.22)
MSE+Consist. (Orig. BRITS)	BRITS	0.36(0.26)	0.20(0.21)	0.49(0.35)	0.27(0.25)

BRITS as the default.

As for *Training Objective*, DRIO outperforms all the other objectives with BRITS backbone with smaller mean and standard deviation in all four metrics. DRIO establishes lower MSE (0.33 vs. 0.34) and W2 (0.18 vs. 0.19) compared to pure MSE training under MCAR, with larger gains under MNAR. Since we keep $\alpha < 1$, these results indicate that the robust regularizer indeed benefits MTS imputation task by including distributional alignment into learning objective. The original BRITS objective (MSE + consistency) performs worse than both, suggesting the consistency term introduces unnecessary constraints. Notably, using balanced Sinkhorn Divergence (BSH-DRIO) performs substantially worse in all metrics, which indicates the importance of allowing mass imbalance arising from missing data.

Cross-Validation Strategy. A key challenge in imputation is hyperparameter selection without access to ground truth missing values. We compare three strategies: (i) *Ground Truth Missingness CV* (oracle, not deployable), which validates on artificially masked entries where ground truth is available; (ii) *Reconstruction-based CV* (ours), which validates on held-out *observed* entries, leveraging the principle that accurate reconstruction of observed data reflects learned spatiotemporal dependencies that generalize to missing entries; and (iii) *Internal Masking*, a common self-supervised strategy that artificially masks observed entries *during training* [Tashiro et al., 2021]. We tune $\alpha \in \{0.01, 0.25, 0.5, 0.75, 0.99\}$ and $\gamma \in \{0.1, 1.0, 5.0, 10.0\}$ for all three strategies and report test MSE averaged across datasets in Figure 3. Our reconstruction-based CV closely tracks oracle performance across all missing ratios, maintaining less than 5% relative gap in test MSE even at 90% missingness. This confirms its reliability as a deployable proxy for hyperparameter selection. In contrast, internal masking degrades more rapidly, particularly under MNAR where the artificial masks fail to capture the true missingness structure.

5 Conclusion

This paper introduces the **D**istributionally **R**obust **R**egularized **I**mputer **O**bjective (DRIO), a framework for MTS imputation that explicitly addresses distributional mismatch between observed

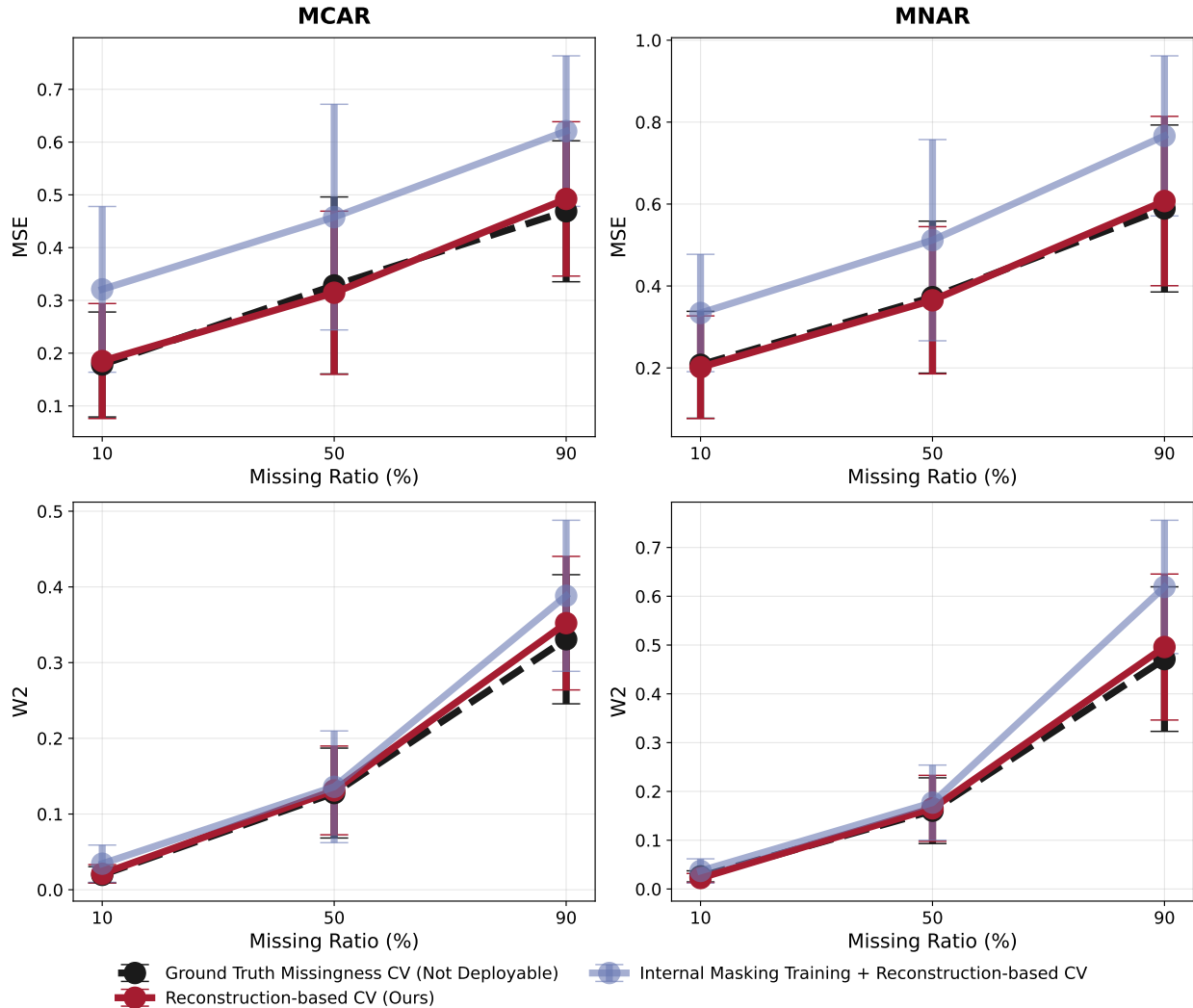


Figure 3: MSE and standard deviation on artificial missing entries in testing set, calculated across all ten datasets, under MCAR and MNAR at various missing ratios.

data and the underlying data manifold. By integrating a Wasserstein ambiguity set into the learning objective, DRIO enables models to hedge against worst-case distributional shifts, mitigating biases from non-stationarity and systematic missingness. Our tractable dual formulation reduces infinite-dimensional optimization to adversarial search over sample trajectories, allowing DRIO to serve as a model-agnostic regularizer compatible with modern deep learning backbones.

Comprehensive evaluations across ten diverse real-world datasets demonstrate that DRIO achieves Pareto-optimal trade-offs between reconstruction accuracy and distributional alignment. Additionally, our reconstruction-based cross-validation strategy provides a reliable, deployable proxy for hyperparameter selection. By shifting from error minimization and pure distributional alignment to distributionally robust regularization, DRIO offers a resilient foundation for MTS imputation.

Acknowledgment

This research was supported in part through research cyberinfrastructure resources and services provided by the Partnership for an Advanced Computing Environment (PACE, PACE [2017]) at the Georgia Institute of Technology, Atlanta, Georgia, USA. Che-Yi Liao is supported by the Seth Bonder Foundation and the George Fellowship. The views expressed herein are those of the authors and do not necessarily reflect those of the Foundation.

References

Eben Afrifa-Yamoah, Ute A Mueller, Stephen M Taylor, and Aiden J Fisher. Missing data imputation of high-resolution temporal climate time series data. *Meteorological Applications*, 27(1):e1873, 2020.

D. Anguita, Alessandro Ghio, L. Oneto, Xavier Parra, and Jorge Luis Reyes-Ortiz. A public domain dataset for human activity recognition using smartphones. In *The European Symposium on Artificial Neural Networks*, 2013. URL <https://api.semanticscholar.org/CorpusID:6975432>.

Christopher R Bollinger, Barry T Hirsch, Charles M Hokayem, and James P Ziliak. Trouble in the tails: Earnings non-response and response bias across the distribution. In *Annual Meeting of the Society of Labor Economists*. <http://citeseerx.ist.psu.edu/viewdoc/download>, 2014.

Xiaoxuan Cai, Charlotte R Fowler, Li Zeng, Habiballah Rahimi Eichi, Dost Ongur, Lisa Dixon, Justin T Baker, Jukka-Pekka Onnela, and Linda Valeri. Missing data in non-stationary multivariate time series from digital studies in psychiatry. *arXiv preprint arXiv:2506.14946*, 2025.

Wei Cao, Dong Wang, Jian Li, Hao Zhou, Lei Li, and Yitan Li. Brits: Bidirectional recurrent imputation for time series. *Advances in neural information processing systems*, 31, 2018.

Changqing Cheng, Akkarapol Sa-Ngasoongsong, Omer Beyca, Trung Le, Hui Yang, Zhenyu Kong, and Satish TS Buppapatnam. Time series forecasting for nonlinear and non-stationary processes: a review and comparative study. *Iie Transactions*, 47(10):1053–1071, 2015.

Saverio De Vito, Ettore Massera, Marco Piga, Luca Martinotto, and Girolamo Di Francia. On field calibration of an electronic nose for benzene estimation in an urban pollution monitoring scenario. *Sensors and Actuators B: Chemical*, 129(2):750–757, 2008.

Gregory Ditzler, Manuel Roveri, Cesare Alippi, and Robi Polikar. Learning in nonstationary environments: A survey. *IEEE Computational intelligence magazine*, 10(4):12–25, 2015.

Ankit Dixit and Shikha Jain. Contemporary approaches to analyze non-stationary time-series: Some solutions and challenges. *Recent Advances in Computer Science and Communications (Formerly: Recent Patents on Computer Science)*, 16(2):61–80, 2023.

Tlameko Emmanuel, Thabiso Maupong, Dimane Mpoeleng, Thabo Semong, Banyatsang Mphago, and Oteng Tabona. A survey on missing data in machine learning. *Journal of Big data*, 8(1):140, 2021.

Hongfan Gao, Wangmeng Shen, Xiangfei Qiu, Ronghui Xu, Jilin Hu, and Bin Yang. Diffimp: Efficient diffusion model for probabilistic time series imputation with bidirectional mamba backbone. *arXiv preprint arXiv:2410.13338*, 2024.

Bidisha Ghosh, Biswajit Basu, and Margaret O’Mahony. Multivariate short-term traffic flow forecasting using time-series analysis. *IEEE transactions on intelligent transportation systems*, 10(2):246–254, 2009.

Shengnan Guo, Youfang Lin, Ning Feng, Chao Song, and Huaiyu Wan. Attention based spatial-temporal graph convolutional networks for traffic flow forecasting. *Proceedings of the AAAI Conference on Artificial Intelligence*, 33(01):922–929, Jul. 2019. doi: 10.1609/aaai.v33i01.3301922. URL <https://ojs.aaai.org/index.php/AAAI/article/view/3881>.

James D Hamilton. *Time series analysis*. Princeton university press, 2020.

Nathaniel E Helwig, K Alex Shorter, Ping Ma, and Elizabeth T Hsiao-Wecksler. Smoothing spline analysis of variance models: A new tool for the analysis of cyclic biomechanical data. *Journal of biomechanics*, 49(14):3216–3222, 2016.

Ehsan Hoseinzade and Saman Haratizadeh. Cnnpred: Cnn-based stock market prediction using a diverse set of variables. *Expert Systems with Applications*, 129:273–285, 2019.

Thomas W Hsiao, Che-Yi Liao, Lance A Waller, and Kamran Paynabar. Balancing access, precision, and equity in adaptive test site allocation with an application to covid-19 in atlanta, georgia. *Scientific Reports*, 15(1):32775, 2025.

Shuo-Chieh Huang, Tengyuan Liang, and Ruey S. Tsay. Temporal wasserstein imputation: A versatile method for time series imputation, 2025. URL <https://arxiv.org/abs/2411.02811>.

Niels Bruun Ipsen, Pierre-Alexandre Mattei, and Jes Frellsen. not-miiae: Deep generative modelling with missing not at random data. *arXiv preprint arXiv:2006.12871*, 2020.

Gebhard Kirchgässner, Jürgen Wolters, and Uwe Hassler. *Introduction to modern time series analysis*. Springer Science & Business Media, 2012.

Huiping Li, Meng Li, Xi Lin, Fang He, and Yinhai Wang. A spatiotemporal approach for traffic data imputation with complicated missing patterns. *Transportation research part C: emerging technologies*, 119:102730, 2020.

Jie Li, Weijie Ren, and Min Han. Variational auto-encoders based on the shift correction for imputation of specific missing in multivariate time series. *Measurement*, 186:110055, 2021. doi: 10.1016/j.measurement.2021.110055. URL <https://www.sciencedirect.com/science/article/pii/S0263224121009805>.

Xuan Liang, Tao Zou, Bin Guo, Shuo Li, Haozhe Zhang, Shuyi Zhang, Hui Huang, and Song Xi Chen. Assessing beijing’s pm2. 5 pollution: severity, weather impact, apec and winter heating. *Proceedings of the Royal Society A: Mathematical, Physical and Engineering Sciences*, 471(2182):20150257, 2015.

Che-Yi Liao, Gian-Gabriel P Garcia, Catherine DiGennaro, and Mohammad S Jalali. Racial disparities in opioid overdose deaths in massachusetts. *JAMA Network Open*, 5(4):e229081–e229081, 2022.

Che-Yi Liao, Peiliang Bai, Lance A Waller, and Kamran Paynabar. Estimating hidden epidemic: A bayesian spatiotemporal compartmental modeling approach. *INFORMS Journal on Data Science*, 4(3):230–247, 2025a.

Che-Yi Liao, Zheng Dong, Gian-Gabriel P Garcia, Kamran Paynabar, Yao Xie, and Mohammad S Jalali. Tides need stemmed: A locally operating spatiotemporal mutually exciting point process

with dynamic network for improving opioid overdose death prediction. *Manufacturing & Service Operations Management*, 2025b.

Che-Yi Liao, Esmaeil Keyvanshokooh, and Gian-Gabriel Garcia. Constraint-aware self-improving large language model for clinical role model generation. *Available at SSRN 5642250*, 2025c.

Qian Ma, Yu Gu, Wang-Chien Lee, Ge Yu, Hongbo Liu, and Xindong Wu. Remian: real-time and error-tolerant missing value imputation. *ACM Transactions on Knowledge Discovery from Data (TKDD)*, 14(6):1–38, 2020.

Ivan Marisca, Andrea Cini, and Cesare Alippi. Learning to reconstruct missing data from spatiotemporal graphs with sparse observations. *Advances in neural information processing systems*, 35: 32069–32082, 2022.

Pierre-Alexandre Mattei and Jes Frellsen. Miwae: Deep generative modelling and imputation of incomplete data sets. In *International conference on machine learning*, pages 4413–4423. PMLR, 2019.

Boris Muzellec, Julie Josse, Claire Boyer, and Marco Cuturi. Missing data imputation using optimal transport. In *International Conference on Machine Learning*, pages 7130–7140. PMLR, 2020.

PACE. *Partnership for an Advanced Computing Environment (PACE)*, 2017. URL <http://www.pace.gatech.edu>.

Tra My Pham, Nikolaos Pandis, and Ian R White. Missing data, part 2. missing data mechanisms: Missing completely at random, missing at random, missing not at random, and why they matter. *American journal of orthodontics and dentofacial orthopedics*, 162(1):138–139, 2022.

Moamar Sayed-Mouchaweh and Edwin Lughofer. *Learning in non-stationary environments: methods and applications*. Springer Science & Business Media, 2012.

Thibault Séjourné, Jean Feydy, François-Xavier Vialard, Alain Trouvé, and Gabriel Peyré. Sinkhorn divergences for unbalanced optimal transport. *arXiv preprint arXiv:1910.12958*, 2019.

Guojiang Shen, Wenfeng Zhou, Wenyi Zhang, Nali Liu, Zhi Liu, and Xiangjie Kong. Bidirectional spatial-temporal traffic data imputation via graph attention recurrent neural network. *Neurocomputing*, 531:151–162, 2023.

Qiuiling Suo, Weida Zhong, Guangxu Xun, Jianhui Sun, Changyou Chen, and Aidong Zhang. Glima: Global and local time series imputation with multi-directional attention learning. In *2020 IEEE International Conference on Big Data (Big Data)*, pages 798–807. IEEE, 2020.

Yusuke Tashiro, Jiaming Song, Yang Song, and Stefano Ermon. Csdì: Conditional score-based diffusion models for probabilistic time series imputation. *Advances in neural information processing systems*, 34:24804–24816, 2021.

Nguyen Tran, Oleksii Abramenco, and Alexander Jung. On the sample complexity of graphical model selection from non-stationary samples. *IEEE Transactions on Signal Processing*, 68:17–32, 2019.

Cédric Villani et al. *Optimal transport: old and new*, volume 338. Springer, 2008.

Hao Wang, Haoxuan Li, Xu Chen, Mingming Gong, Zhichao Chen, et al. Optimal transport for time series imputation. In *The Thirteenth International Conference on Learning Representations*, 2025a.

Jie Wang, Rui Gao, and Yao Xie. Sinkhorn distributionally robust optimization. *Operations Research*, 2025b.

Yang Yang, Che-Yi Liao, Esmaeil Keyvanshokoh, Hui Shao, Mary Beth Weber, Francisco J Pasquel, and Gian-Gabriel P Garcia. A responsible framework for assessing, selecting, and explaining machine learning models in cardiovascular disease outcomes among people with type 2 diabetes: Methodology and validation study. *JMIR Medical Informatics*, 13:e66200, 2025.

Yongchao Ye, Shiyao Zhang, and James JQ Yu. Spatial-temporal traffic data imputation via graph attention convolutional network. In *International Conference on artificial neural networks*, pages 241–252. Springer, 2021.

Jinsung Yoon, James Jordon, and Mihaela Schaar. Gain: Missing data imputation using generative adversarial nets. In *International conference on machine learning*, pages 5689–5698. PMLR, 2018.

Kai Zhang, Qinmin Yang, Chao Li, Xin Sun, and Jiming Chen. Missing data recovery methods on multivariate time series in iot: A comprehensive survey. *IEEE Communications Surveys & Tutorials*, 2025.

Andrey Ziyatdinov, Jordi Fonollosa, Luis Fernández, Agustín Gutierrez-Gálvez, Santiago Marco, and Alexandre Perera. Bioinspired early detection through gas flow modulation in chemo-sensory systems. *Sensors and Actuators B: Chemical*, 206:538–547, 2015.

A Design Choice

A.1 Loss Function Construction

We now formally define the divergence metric $S_{\epsilon,\tau}$ used in our objective (2). Let $\mathcal{Z} = \mathbb{R}^{D \times T}$ denote the feature-temporal space of the observed data dimension. For any two probability measures $\mu, \nu \in \mathcal{P}(\mathcal{Z})$, the entropic unbalanced transport cost $W_{\epsilon,\tau}$ is defined as the solution to the minimization problem over all positive transport plans π :

$$W_{\epsilon,\tau}(\mu, \nu) := \inf_{\pi \geq 0} \left\{ \int_{\mathcal{Z}^2} d(\mathbf{x}, \mathbf{z}) d\pi(\mathbf{x}, \mathbf{z}) + \epsilon \text{KL}(\pi | \mu \otimes \nu) + \tau(\text{KL}(\pi_1 | \mu) + \text{KL}(\pi_2 | \nu)) \right\},$$

where π is a positive Radon measure on $\mathcal{Z} \times \mathcal{Z}$ with marginals π_1 and π_2 , $d(\mathbf{x}, \mathbf{z}) = \|\mathbf{x} - \mathbf{z}\|_F^2$ is the ground metric, and $\text{KL}(\cdot | \cdot)$ denotes the Kullback-Leibler divergence. Here, $\epsilon > 0$ is the entropic regularization coefficient that smooths the transport plan, and $\tau > 0$ is the marginal relaxation parameter that allows creating and destroying local mass.

The **Unbalanced Sinkhorn Divergence** is then defined via the debiasing formula, i.e.,

$$S_{\epsilon,\tau}(\mu, \nu) := W_{\epsilon,\tau}(\mu, \nu) - \frac{1}{2} (W_{\epsilon,\tau}(\mu, \mu) + W_{\epsilon,\tau}(\nu, \nu)).$$

The **Balanced Sinkhorn Divergence** is recovered as $\tau \rightarrow \infty$, which enforces strict marginal constraints. In this case, the transport plan π must belong to the set of couplings $\Pi(\mu, \nu) = \{\pi \geq 0 : \pi_1 = \mu, \pi_2 = \nu\}$, and the entropic transport cost simplifies to:

$$W_{\epsilon}(\mu, \nu) := \inf_{\pi \in \Pi(\mu, \nu)} \left\{ \int_{\mathcal{Z}^2} d(\mathbf{x}, \mathbf{z}) d\pi(\mathbf{x}, \mathbf{z}) + \epsilon \text{KL}(\pi | \mu \otimes \nu) \right\}.$$

The balanced Sinkhorn divergence is then $S_{\epsilon}(\mu, \nu) := W_{\epsilon}(\mu, \nu) - \frac{1}{2}(W_{\epsilon}(\mu, \mu) + W_{\epsilon}(\nu, \nu))$. We use this balanced formulation (BSH-DRIO) in our ablation study to analyze the effect of marginal relaxation.

Why Wasserstein-based Divergence? We employ an Optimal Transport (Wasserstein-based) loss function rather than classical divergences because standard metrics fail to capture the geometric properties of the support. Point-wise metrics like MSE assume unimodal noise distributions and tend to blur predictions in high-uncertainty regions. Likelihood-based objectives (such as KL divergence used in Variational Autoencoders) suffer from vanishing gradients when the support of the model distribution and the data distribution do not overlap [Villani et al., 2008, Wang et al., 2025a]. In contrast, Optimal Transport provides meaningful gradients even when supports are disjoint by measuring the work required to transport mass, ensuring robust learning signals throughout the optimization process.

Why Sinkhorn Divergence? While the Wasserstein geometry is ideal, computing the exact Wasserstein distance involves solving a network flow linear program, which has super-cubic complexity $O(n^3 \log n)$ and is non-differentiable. This prohibits its use in the inner loop of a deep learning framework. To resolve this, we utilize the Sinkhorn Divergence. By adding entropic regularization, the problem becomes strictly convex and solvable in $O(n^2)$ time Villani et al. [2008], Wang et al. [2025b]. Crucially, the Sinkhorn Divergence is smooth and differentiable, allowing for stable backpropagation of gradients to the generator parameters θ .

Why Unbalanced Sinkhorn Divergence? We employ the *unbalanced* formulation specifically to mitigate the systematic support bias caused by MNAR mechanisms. Standard Wasserstein distances

(and balanced Sinkhorn) enforce strict conservation of mass, requiring the integral of the imputed distribution to exactly match that of the empirical reference. When the observed data has truncated support (e.g., missing tails), this constraint distort the probability mass from the reliable observed to fill the unobserved voids. In contrast, the Unbalanced Sinkhorn Divergence relaxes the marginal constraints via the parameter τ . This allows the transport plan to **create or destroy mass** locally, which is critical for non-stationary environments, as it allows the imputer G_{θ} to instantaneously create new modes, with a penalty, without strictly following the global mass balance constraint Séjourné et al. [2019].

B Theoretical Result

Proof of Theorem 3.2.

By the definition of the ambiguity set (1), the worst-case divergence problem can be rewritten as:

$$\begin{aligned} & \sup_{\mathbb{Q} \in \mathcal{P}(\mathbb{R}^{D \times T})} S_{\epsilon, \tau}(\mathbb{Q}, \hat{\mathbb{P}}_{\theta}) \\ \text{subject to } & \inf_{\pi \in \Pi(\hat{\mathbb{P}}_N, \mathbb{Q})} \mathbb{E}_{(\mathbf{X}, \mathbf{Z}) \sim \pi} [c_{\mathbf{X}}(\mathbf{Z})] \leq \rho, \end{aligned} \quad (6)$$

where $\rho \geq 0$. To derive the dual formulation, we aim to establish that the nested maximization over distributions \mathbb{Q} and the inner minimization over couplings π can be unified into a single constrained maximization. Specifically, we first define the maximization problem over the coupling π :

$$\begin{aligned} & \sup_{\pi \in \mathcal{P}(\mathbb{R}^{D \times T} \times \mathbb{R}^{D \times T})} S_{\epsilon, \tau}(\pi_{\mathbf{Z}}, \hat{\mathbb{P}}_{\theta}) \\ \text{subject to } & \mathbb{E}_{(\mathbf{X}, \mathbf{Z}) \sim \pi} [c_{\mathbf{X}}(\mathbf{Z})] \leq \rho \\ & \pi_{\mathbf{X}} = \hat{\mathbb{P}}_N \end{aligned} \quad (7)$$

where $\pi_{\mathbf{X}}$ and $\pi_{\mathbf{Z}}$ represent the first and the second marginal of the coupling π , respectively. Now, we show that (6) is equivalent to (7).

Let V_1 denote the optimal value of the original problem (6) and V_2 denote the optimal value of the reformulated problem (7). First, we start with (7). Consider a feasible coupling π that satisfies the marginal constraint $\pi_{\mathbf{X}} = \hat{\mathbb{P}}_N$ and the budget constraint. Then, the following relationship holds by definition:

$$\rho \geq \mathbb{E}_{(\mathbf{X}, \mathbf{Z}) \sim \pi} [c_{\mathbf{X}}(\mathbf{Z})] \geq \inf_{\pi \in \Pi(\hat{\mathbb{P}}_N, \mathbb{Q})} \mathbb{E}_{(\mathbf{X}, \mathbf{Z}) \sim \pi} [c_{\mathbf{X}}(\mathbf{Z})], \quad (8)$$

where $\mathbb{Q} \in \mathcal{P}(\mathbb{R}^{D \times T})$. Thus, any solution to (7) is feasible in (6), which implies that $V_2 \leq V_1$.

Conversely, consider (6). By definition, the minimum transport cost from $\hat{\mathbb{P}}_N$ to any distribution \mathbb{Q} in the ambiguity set is at most ρ . Let π^* be a coupling representing the optimal transport plan that achieves this minimum cost. Then π^* satisfies $\mathbb{E}_{(\mathbf{X}, \mathbf{Z}) \sim \pi^*} [c_{\mathbf{X}}(\mathbf{Z})] \leq \rho$ with the first marginal $\pi_{\mathbf{X}} = \hat{\mathbb{P}}_N$. Consequently, π^* is a feasible solution to (7), implying $V_1 \leq V_2$. This establishes the equivalence between (6) and (7).

Now, we introduce a Lagrange multiplier $\gamma \geq 0$ to (7) to relax the transport budget constraint, which yields:

$$\sup_{\pi: \pi_{\mathbf{X}} = \hat{\mathbb{P}}_N} \inf_{\gamma \geq 0} \left\{ S_{\epsilon, \tau}(\pi_{\mathbf{Z}}, \hat{\mathbb{P}}_{\theta}) + \gamma \rho - \gamma \mathbb{E}_{(\mathbf{X}, \mathbf{Z}) \sim \pi} [c_{\mathbf{X}}(\mathbf{Z})] \right\}. \quad (9)$$

By rearranging the terms inside the objective and exchanging the order of supremum and infimum in (9), we obtain the dual formulation to the primal worst-case divergence problem:

$$\inf_{\gamma \geq 0} \left\{ \gamma \rho + \sup_{\pi: \pi_{\mathbf{X}} = \widehat{\mathbb{P}}_N} \left(S_{\epsilon, \tau} \left(\pi_{\mathbf{Z}}, \widehat{\mathbb{P}}_{\boldsymbol{\theta}} \right) - \gamma \mathbb{E}_{(\mathbf{X}, \mathbf{Z}) \sim \pi} [c_{\mathbf{X}}(\mathbf{Z})] \right) \right\}. \quad (10)$$

By weak duality, the formulation (10) is an upper bound on the primal objective. We note that the Unbalanced Sinkhorn Divergence $S_{\epsilon, \tau}(\cdot, \widehat{\mathbb{P}}_{\boldsymbol{\theta}})$ is a convex functional with respect to the input measure. Consequently, the standard Minimax Theorem (which requires a concave-convex structure) does not guarantee strict equality for this swap of the infimum and supremum. However, establishing (10) as an upper bound is sufficient for our distributionally robust framework. From theoretical perspective, minimizing this dual objective guarantees that we minimize a conservative surrogate of the worst-case risk. Specifically, if the model is robust against this dual upper bound, it is by definition robust against the primal worst-case scenario. From practical implementation perspective, the transport budget ρ and the Lagrange multiplier γ are tuned by cross-validation on a certain selection criteria, e.g., mean square error on validation data, which resulted in optimized performance based on our dual formulation.

We now proceed to simplify the inner maximization of this upper bound. Although the outer duality gap exists, we show next that the inner search for the worst-case measure is exact. Note that in the inner maximization, the first marginal of π is fixed to the discrete empirical distribution $\widehat{\mathbb{P}}_N = \frac{1}{N} \sum \delta_{\overline{\mathbf{X}}^{(i)}}$. Therefore, by the disintegration formula, any feasible coupling π can be uniquely decomposed into a mixture of N conditional distributions. That is, for any feasible π in (10), we have

$$\pi = \int \delta_{\mathbf{X}} \otimes \pi(\cdot | \mathbf{X}) d\widehat{\mathbb{P}}_N(\mathbf{X}) = \frac{1}{N} \sum_{i=1}^N \delta_{\overline{\mathbf{X}}^{(i)}} \otimes \pi^{(i)}(\mathbf{Z}), \quad (11)$$

where $\pi^{(i)}(\mathbf{Z})$ denotes the conditional distribution of the adversary given sample $\overline{\mathbf{X}}^{(i)}$. Then, we have:

$$d\pi(\mathbf{X}, \mathbf{Z}) = \frac{1}{N} \sum_{i=1}^N \delta_{\overline{\mathbf{X}}^{(i)}} d\mathbf{X} \otimes d\pi^{(i)}(\mathbf{Z}).$$

Consequently, the expected ground cost over the coupling π in (10) can be simplified to an expectation conditional on the samples. That is,

$$\mathbb{E}_{(\mathbf{X}, \mathbf{Z}) \sim \pi} [c_{\mathbf{X}}(\mathbf{Z})] = \int c_{\mathbf{X}}(\mathbf{Z}) d\pi(\mathbf{X}, \mathbf{Z}) \quad (12)$$

$$= \int c_{\mathbf{X}}(\mathbf{Z}) \left(\frac{1}{N} \sum_{i=1}^N \delta_{\overline{\mathbf{X}}^{(i)}}(d\mathbf{X}) \otimes d\pi^{(i)}(\mathbf{Z}) \right) \quad (13)$$

$$= \frac{1}{N} \sum_{i=1}^N \int_{\mathbf{Z}} \left(\int_{\mathbf{X}} c_{\mathbf{X}}(\mathbf{Z}) \delta_{\overline{\mathbf{X}}^{(i)}}(d\mathbf{X}) \right) d\pi^{(i)}(\mathbf{Z}) \quad (14)$$

$$= \frac{1}{N} \sum_{i=1}^N \int_{\mathbf{Z}} c_{\overline{\mathbf{X}}^{(i)}}(\mathbf{Z}) d\pi^{(i)}(\mathbf{Z}). \quad (15)$$

Next, for the Sinkhorn term in (10), we further rewrite the second marginal $\pi_{\mathbf{Z}}$ of the coupling π

by marginalization using results from (11):

$$\pi_{\mathbf{Z}} = \int \pi \, d\mathbf{X} = \int \frac{1}{N} \sum_{i=1}^N \delta_{\bar{\mathbf{X}}^{(i)}} \otimes \pi^{(i)}(\mathbf{Z}) \, d\mathbf{X} \quad (16)$$

$$= \frac{1}{N} \sum_{i=1}^N \int \delta_{\bar{\mathbf{X}}^{(i)}} \otimes \pi^{(i)}(\mathbf{Z}) \, d\mathbf{X} \quad (17)$$

$$= \frac{1}{N} \sum_{i=1}^N \pi^{(i)}. \quad (18)$$

Therefore, inserting (15) and (18) into (10), we know that maximizing over the joint coupling π is equivalent to maximizing over the set of conditional distributions $\{\pi^{(i)}\}_{i=1}^N$, which implies that (10) is equivalent to:

$$\inf_{\gamma \geq 0} \left\{ \gamma \rho + \sup_{\{\pi^{(i)}\}_{i=1}^N} \left(S_{\epsilon, \tau} \left(\frac{1}{N} \sum_{i=1}^N \pi^{(i)}, \hat{\mathbb{P}}_{\boldsymbol{\theta}} \right) - \frac{\gamma}{N} \sum_{i=1}^N \int c_{\bar{\mathbf{X}}^{(i)}}(\mathbf{Z}) \, d\pi^{(i)}(\mathbf{Z}) \right) \right\}. \quad (19)$$

Next, we show that the search over the couplings is equivalent to search over deterministic adversary trajectories $\zeta^{(i)}$. To formalize this insight, we note that the Unbalanced Sinkhorn divergence $S_{\epsilon, \tau}(\cdot, \hat{\mathbb{P}}_{\boldsymbol{\theta}})$ is a convex functional with respect to the input measure. Moreover, by definition of the ambiguity set (1), the quadratic ground cost effectively ensures that the optimal adversarial trajectory remain within a bounded convex region around the observed data. Therefore, we can apply the first-order optimality conditions for convex maximization. Specifically, a solution y^* is a global maximizer for a convex function g over a convex set if and only if it maximizes the linear inner product with its subgradient evaluated at that optimal point, i.e., $y^* \in \arg \sup_y g(y) \iff y^* \in \arg \sup_y \langle \nabla g(y^*), y \rangle$.

Defining $\varphi(\cdot) = \nabla_{\mu} S_{\epsilon, \tau}(\mu, \hat{\mathbb{P}}_{\boldsymbol{\theta}})$ and applying this property, the Sinkhorn term in (19) becomes:

$$\begin{aligned} \arg \sup_{\{\pi^{(i)}\}_{i=1}^N} S_{\epsilon, \tau} \left(\frac{1}{N} \sum_{i=1}^N \pi^{(i)}, \hat{\mathbb{P}}_{\boldsymbol{\theta}} \right) &= \arg \sup_{\{\pi^{(i)}\}_{i=1}^N} \left\langle \varphi, \frac{1}{N} \sum_{i=1}^N \pi^{(i)} \right\rangle \\ &= \arg \sup_{\{\pi^{(i)}\}_{i=1}^N} \int \varphi(\mathbf{Z}) \, d \left(\frac{1}{N} \sum_{i=1}^N \pi^{(i)} \right) (\mathbf{Z}) \\ &= \arg \sup_{\{\pi^{(i)}\}_{i=1}^N} \sum_{i=1}^N \int \varphi(\mathbf{Z}) \, d\pi^{(i)}(\mathbf{Z}). \end{aligned} \quad (20)$$

Note that the constant factor $1/N$ is omitted in the final step as it does not affect the argument of the supremum. This exact reformulation shows that finding the optimal distribution is equivalent to solving N independent linear maximization problems. Combining this result with the cost term, (19) becomes

$$\inf_{\gamma \geq 0} \left\{ \gamma \rho + \sum_{i=1}^N \sup_{\pi^{(i)}} \int \left(\varphi(\mathbf{Z}) - \frac{\gamma}{N} c_{\bar{\mathbf{X}}^{(i)}}(\mathbf{Z}) \right) \, d\pi^{(i)}(\mathbf{Z}) \right\}. \quad (21)$$

Now, we define $\mathcal{J}^{(i)}(\mathbf{Z}) := \varphi(\mathbf{Z}) - \frac{\gamma}{N} c_{\bar{\mathbf{X}}^{(i)}}(\mathbf{Z})$ and establish that for any solution distribution $\pi^{(i)}$,

the corresponding expectation over $\mathcal{J}^{(i)}$ is upper bounded:

$$\begin{aligned} \int \mathcal{J}^{(i)}(\mathbf{Z}) d\pi^{(i)}(\mathbf{Z}) &\leq \int \left(\sup_{\zeta \in \mathbb{R}^{D \times T}} \mathcal{J}^{(i)}(\zeta) \right) d\pi^{(i)}(\mathbf{Z}) \\ &= \sup_{\zeta \in \mathbb{R}^{D \times T}} \mathcal{J}^{(i)}(\zeta) \left(\int 1 d\pi^{(i)}(\mathbf{Z}) \right) = \sup_{\zeta \in \mathbb{R}^{D \times T}} \mathcal{J}^{(i)}(\zeta). \end{aligned} \quad (22)$$

Since there is no constraints on the conditional distribution $\pi^{(i)}(\mathbf{Z})$, we can define $\zeta_*^{(i)} := \arg \sup_{\zeta} \mathcal{J}^{(i)}(\zeta)$ as the optimal trajectory over $\mathcal{J}^{(i)}$ and pick $\pi^{(i)}(\mathbf{Z})$ to be the point measure $\delta_{\zeta_*^{(i)}}$. With this choice of the conditional distribution, equality holds for the above expression, as

$$\int \mathcal{J}^{(i)}(\mathbf{Z}) d\delta_{\zeta_*^{(i)}}(\mathbf{Z}) = \mathcal{J}^{(i)}(\zeta_*^{(i)}) = \sup_{\zeta \in \mathbb{R}^{D \times T}} \mathcal{J}^{(i)}(\zeta). \quad (23)$$

This result implies that the problem reduces to finding the measure $\pi^{(i)}$ for each sample i that maximizes the integrand point-wise. Specifically, the functional optimization problem for the i -th conditional distribution in (21) reduces to:

$$\sum_{i=1}^N \sup_{\pi^{(i)}} \int \left(\varphi(\mathbf{Z}) - \frac{\gamma}{N} c_{\bar{\mathbf{X}}^{(i)}}(\mathbf{Z}) \right) d\pi^{(i)}(\mathbf{Z}) = \sum_{i=1}^N \sup_{\zeta^{(i)} \in \mathbb{R}^{D \times T}} \left(\varphi(\zeta^{(i)}) - \frac{\gamma}{N} c_{\bar{\mathbf{X}}^{(i)}}(\zeta^{(i)}) \right). \quad (24)$$

In other words, the optimal conditional distributions are point masses, i.e., $\pi_*^{(i)} = \delta_{\zeta_*^{(i)}}$, which further implies that solution worst-case distribution to the dual problem can be obtained by substituting these back into the definition of the marginal of the adversary trajectories. With this insight, we revisit the dual formulation (19). We define the each conditional distribution as the empirical distribution of the adversaries as $\pi^{(i)} := \delta_{\zeta^{(i)}}$ and the global solution distribution as $\hat{\mathbb{Q}}_{\mathcal{Z}} := \sum_{i=1}^N \pi^{(i)}/N$. Then, solving the dual formulation (19) is equivalent to solving:

$$\inf_{\gamma \geq 0} \left\{ \gamma \rho + \sup_{\mathcal{Z}} \left(S_{\epsilon, \tau} \left(\hat{\mathbb{Q}}_{\mathcal{Z}}, \hat{\mathbb{P}}_{\theta} \right) - \gamma C_{\mathcal{Z}} \right) \right\}, \quad (25)$$

where $\mathcal{Z} = \{\zeta^{(i)}\}_{i=1}^N$ and $C_{\mathcal{Z}} := \sum_{i=1}^N c_{\bar{\mathbf{X}}^{(i)}}(\zeta^{(i)})/N$.

This completes the proof. \square

C Experimental Details

C.1 Datasets

We evaluate on ten multivariate time series datasets spanning diverse domains: healthcare, transportation, environmental monitoring, industrial systems, and human activity. The C-MAPSS dataset is obtained from NASA, PhysioNet from the PhysioNet Challenge 2012, and the remaining eight datasets from the UCI Machine Learning Repository. Below we describe each dataset and our preprocessing procedures. In model training, validation, and testing pipeline, we follow Tashiro et al. [2021] and structure all datasets as three-dimensional tensors of shape (N, T, D) representing samples, time steps, and features, respectively. Note that the exchange of temporal and feature dimensions does not affect our theory and algorithm as one just needs to swap the indices during computation.

CNNpred [Hoseinzade and Haratizadeh, 2019]. UCI stock market data combining 5 US indices (S&P 500, NASDAQ, DJI, Russell, NYSE) from 2010–2017. Features include technical indicators, commodity prices, treasury rates, and global market indices. We segment each index into non-overlapping quarterly chunks of 60 trading days, treating each chunk as an independent sample. The resulting shape is $(165, 60, 78)$ representing 165 quarters pooled across the 5 indices.

PEMS04 & PEMS08 [Guo et al., 2019]. California highway traffic sensor data from Districts 4 and 8. Raw measurements (flow, occupancy, speed) are collected at 5-minute intervals. We aggregate to daily resolution by summing flow counts and averaging occupancy and speed, treating each sensor as an independent sample with days as the temporal dimension. The resulting shapes are $(170, 62, 3)$ for PEMS08 and $(307, 59, 3)$ for PEMS04, representing 170 and 307 sensors over 62 and 59 days, respectively.

PM2.5 [Liang et al., 2015]. Beijing air quality data (2010–2014) with hourly measurements of PM2.5 concentration and meteorological variables (dew point, temperature, pressure, wind speed, cumulative snow, cumulative rain). We structure the data with weeks as the sample unit, where each week contains 168 hourly observations. The resulting shape is $(260, 168, 7)$ representing 260 weeks.

Gas Sensor [Ziyatdinov et al., 2015]. UCI Gas Sensor Array data from 58 experiments exposing 16 metal-oxide sensors to acetone/ethanol mixtures under flow modulation. Each experiment contains 7500 time steps recorded at 25Hz. We downsample by a factor of 10 to reduce temporal redundancy, then segment each experiment into 5 non-overlapping chunks of 150 time steps. Each chunk is treated as an independent sample. The resulting shape is $(290, 150, 16)$ representing $58 \times 5 = 290$ chunks.

Gait [Helwig et al., 2016]. UCI Multivariate Gait data from 10 subjects walking under 3 conditions (normal, knee-braced, ankle-braced) with 10 gait cycles per condition. Each gait cycle is time-normalized to 101 points spanning 0–100% of the gait phase, and treated as one sample. The 6 features are bilateral joint angles: ankle, hip, and knee for both left and right legs. The resulting shape is $(300, 101, 6)$ representing $10 \times 3 \times 10 = 300$ gait cycles.

C-MAPSS ([url: https://data.nasa.gov/dataset/cmapss-jet-engine-simulated-data](https://data.nasa.gov/dataset/cmapss-jet-engine-simulated-data)). NASA turbofan engine degradation simulation combining the FD001–FD004 subsets. Each engine’s operational lifetime constitutes one sample, with operational cycles as the temporal dimension. To ensure uniform sequence length, we retain only engines with at least 207 cycles (the median across all subsets) and truncate to the first 207 cycles. The 21 features comprise sensor measurements tracking engine health degradation. The resulting shape is $(359, 207, 21)$ representing 359 engines.

Air Quality [De Vito et al., 2008]. UCI air quality data from an Italian city (March 2004 – February 2005) with hourly measurements from metal-oxide gas sensors and co-located reference analyzers. Features include pollutant concentrations (CO, NO_x, NO₂, benzene, ozone) and environmental variables (temperature, relative humidity, absolute humidity). We structure the data with days as the sample unit, where each day contains 24 hourly observations. This dataset contains natural missing values marked in the original data. The resulting shape is $(389, 24, 13)$ representing 389 days.

HAR [Anguita et al., 2013]. UCI Human Activity Recognition dataset containing smartphone inertial sensor readings from 30 subjects performing 6 activities. Each sample corresponds to a 2.56-second sliding window sampled at 50Hz, yielding 128 time steps. The 9 features comprise triaxial body acceleration, body gyroscope, and total acceleration. We use the test partition, resulting in shape (2947, 128, 9).

PhysioNet ([url: `https://physionet.org/content/challenge-2012/1.0.0/`](https://physionet.org/content/challenge-2012/1.0.0/)). ICU patient monitoring data from the PhysioNet Challenge 2012. Each patient’s 48-hour ICU stay is treated as one sample, with 35 clinical variables (vital signs, lab values) aggregated to hourly resolution. This dataset exhibits substantial natural missingness due to irregular clinical measurement schedules. The resulting shape is (4000, 48, 35) where 4000 is the number of patients.

C.2 Missing Data Generation Mechanisms

We implement two artificial missingness mechanisms to evaluate imputation methods.

Missing Completely at Random (MCAR). Under MCAR, the probability of a value being missing is independent of both the observed and unobserved data. For each sample i , we generate the ground-truth mask $\mathbf{M}_{\text{gt}}^{(i)}$ according to the raw observation mask $\mathbf{M}^{(i)}$ and the target missing ratio r . Specifically, we first identify all observed indices $\mathcal{I}^{(i)} = \{(t, d) : \mathbf{M}_{t,d}^{(i)} = 1\}$, then uniformly sample $\lfloor r \cdot |\mathcal{I}^{(i)}| \rfloor$ indices to mask. The ground-truth mask thus is set to $\mathbf{M}_{\text{gt},d,t}^{(i)} = 0$ for sampled indices and $\mathbf{M}_{\text{gt},d,t}^{(i)} = 1$ otherwise.

Missing Not at Random (MNAR). Under MNAR, the probability of missingness depends on the unobserved value itself. We implement a mechanism where extreme values (in either direction) are more likely to be missing. Specifically, for each entry with value $\mathbf{X}_{d,t}^{(i)}$, we compute its z-score $z_{d,t}^{(i)} = (\mathbf{X}_{d,t}^{(i)} - \bar{x}_d)/\sigma_d$ where \bar{x}_d and σ_d are feature mean and standard deviation across sample-temporal space. The missing weigh for each observed value is then given by $w_{t,d}^{(i)} = \Phi(|z_{t,d}^{(i)}|)$, where $\Phi(\cdot)$ is the CDF of the standard normal distribution. Then, we normalize these weights across samples to obtain the missing probabilities $p_{t,d}^{(i)} = w_{t,d}^{(i)} / \sum_i \sum_{(t',d') \in \mathcal{I}^{(i)}} p_{t',d'}^{(i)}$. Consequently extreme values have a higher missing probability, a realistic scenario in many domains such as sensor saturation or reporting bias. Finally, we sample $\lfloor r \cdot |\mathcal{I}^{(i)}| \rfloor$ indices without replacement according to missing ratio r and set the ground truth mask $\mathbf{M}_{\text{gt},d,t}^{(i)} = 0$ for sampled indices and $\mathbf{M}_{\text{gt},d,t}^{(i)} = 1$ otherwise.

Missingness Settings. We evaluate at three missing ratios $r \in \{0.1, 0.5, 0.9\}$, representing easy, moderate, and challenging imputation scenarios. For datasets with natural missingness (e.g., PhysioNet, Air Quality), the synthetic missing mask is applied on top of the original observed values, and evaluation is performed only on the synthetically masked entries where ground truth is available. To ensure reproducibility and fair comparison, we use deterministic seed generation to guarantee identical test sets across different experimental configurations.

C.3 Hyperparameter Configuration for DRIO

Our proposed training objective (DRIO) incorporates four hyperparameters: the unbalanced Sinkhorn divergence parameters (ε and τ) and the distributional robustness parameters (α and γ). While

performing cross-validation across the full four-dimensional parameter space could potentially enhance model performance, it incurs prohibitive computational overhead. We therefore fix the divergence parameters and employ cross-validation exclusively to tune α and γ .

Unbalanced Sinkhorn Divergence Parameters (ϵ, τ). The divergence parameters determine the functional structure of the optimization landscape. The entropic regularization ϵ smooths the transport plan and ensures non-vanishing gradients, while τ controls the penalty for local mass creation and destruction. Since τ functionally determines the cost of violating marginal constraints, its role overlaps with γ , which sets the total transport budget. Fixing ϵ and τ thus avoids redundant parameter tuning while ensuring numerical stability. Consequently, we fix $\tau = 10$ to impose a soft constraint that encourages mass conservation between the imputed and adversarial distributions, while still accommodating local mass fluctuations inherent to non-stationary data imputation.

As for ϵ , we adopt the adaptive scheme from Muzellec et al. [2020]. That is, given a data batch, we compute pairwise squared Euclidean distances between samples, then set $\epsilon = 0.05 \cdot q_{0.5}$, where $q_{0.5}$ is the median of the non-zero distances. This ensures ϵ scales appropriately with data geometry across datasets without manual tuning. This strategy effectively fixes the divergence landscape, allowing us to efficiently optimize the trade-off between fidelity and robustness via α and γ . In the following, we detail the cross-validation procedure for these parameters.

Cross-Validation for Robustness Parameters (α, γ). For each hyperparameter combination, we train the imputer using (DROI) on the training set and evaluate performance on the validation set. Following standard practice in imputation, we compute the mean squared error on the *observed entries* of the validation data as the selection criterion, choosing the (α, γ) pair that achieves the lowest validation loss. Throughout this manuscript, we consider hyperparameter grid: $\alpha \in \{0.01, 0.25, 0.5, 0.75, 0.99\}$ and $\gamma \in \{0.1, 1.0, 5.0, 10.0\}$.

This validation strategy requires the imputer to learn the underlying spatiotemporal dependencies between features, and these correlations remain consistent across both observed and unobserved entries within each sample. By evaluating reconstruction quality on held-out observed entries, we test the model’s ability to leverage learned dependencies for imputation without requiring access to ground-truth missing values. The selected (α, γ) pair thus balances reconstruction accuracy and robustness to distribution shift, avoiding overfitting to potentially biased empirical densities.

C.4 Error Metric

Beyond point-wise metrics (MSE), we evaluate distributional alignment using the Wasserstein-2 distance between the completed dataset and ground truth at missing entries. We aggregate all imputed values (and ground truths) at missing entries across samples, features, and time steps into one-dimensional empirical distributions and compute the closed-form 1D Wasserstein-2 distance via quantile matching:

$$W_2 = \sqrt{\frac{1}{n} \sum_{i=1}^n \left(\hat{y}_{(i)} - y_{(i)}^* \right)^2}, \quad (26)$$

where $\hat{y}_{(i)}$ and $y_{(i)}^*$ are the i^{th} order statistics of the flattened imputations and ground-truth values, respectively. This metric captures whether the imputation preserves the overall data distribution, complementing MSE which only measures point-wise accuracy.

C.5 Configuration for Ablation Study

C.5.1 Model Backbone Architecture

As for model backbone, we consider four standard neural network backbone architectures of varying complexity in ablation study in §4. All models take as input the observed data $\mathbf{X}_{\text{obs}} \in \mathbb{R}^{D \times T}$ concatenated with the observation mask $\mathbf{M} \in \{0, 1\}^{D \times T}$, and output imputed values $\widehat{\mathbf{X}} \in \mathbb{R}^{D \times T}$. Missing entries in the input are initialized via mean imputation computed per (d, t) position across the batch. Table 4 summarizes the hyperparameter settings.

Table 4: Backbone architecture hyperparameters.

Model	Hidden Dimension	Layers	Heads	Feed-Forward Dimension	Dropout	Parameters
MLP	128	3	—	—	0.1	~50K
LSTM	128	2	—	—	0.1	~400K
GAT	128	2	4	—	0.1	~150K
ST-Transformer	128	4	8	512	0.1	~2M

Multi-Layer Perceptron (MLP). A simple feedforward network that processes each time step independently. The input, i.e., concatenated data and mask at time t , is passes through 3 fully-connected layers with hidden dimension 128 and Rectified Linear Unit (ReLU) activations, outputting an \mathbb{R}^D vector. This baseline captures no temporal dependencies as it processes each timestamp separately.

Long Short-Term Memory (LSTM). We implement a bidirectional LSTM that captures temporal dependencies. The input sequence $[\mathbf{X}_{\text{obs}}; \mathbf{M}] \in \mathbb{R}^{T \times 2D}$ is first projected to dimension 128, then processed by a 2-layer bidirectional LSTM with hidden size 128. The concatenated forward and backward hidden states (dimension 256) are projected back to D features. This architecture captures long-range temporal patterns but treats features independently within each LSTM cell.

GAT (Graph Attention Network). A graph neural network that models inter-feature dependencies. Features are treated as nodes in a fully-connected graph. The input $[\mathbf{X}_{\text{obs}}; \mathbf{M}] \in \mathbb{R}^{D \times 2T}$ (concatenated across time) is projected to dimension 128, then processed by 2 layers of multi-head graph attention with 4 heads each (32 dimensions per head). This architecture captures cross-feature correlations but processes the temporal dimension only through the input/output projections.

Spatiotemporal Transformer (STT). Our primary architecture employing factorized attention over both temporal and spatial (feature) dimensions. The input $[\mathbf{X}_{\text{obs}}; \mathbf{M}] \in \mathbb{R}^{D \times T \times 2}$ is projected to dimension 128 with learnable positional encodings for both dimensions. Each of the 4 transformer layers applies both temporal and spatial attention, where temporal attention represents self-attention across T time steps independently for each feature, with complexity $\mathcal{O}(DT^2)$; and spatial attention represents self-attention across D features independently for each time step, with complexity $\mathcal{O}(TD^2)$.

Each attention block uses 8 heads, pre-layer normalization, GELU activation in the feed-forward network (dimension 512), and residual connections. The factorized design reduces complexity from $\mathcal{O}((DT)^2)$ for full attention to $\mathcal{O}(DT^2 + TD^2)$, enabling scalability to larger spatiotemporal grids while capturing both intra-feature temporal dynamics and inter-feature correlations at each time step.

Table 5: Imputation results under MCAR missing mechanism. Values show mean(std) across 10%, 50%, and 90% missing ratios. Imputation results under MCAR missing mechanism. Values are averaged across 10%, 50%, and 90% missing ratios. **Bold** indicates top 3 performance per dataset. nMW is short for notMIWAE. DRIO is paired with BRITS backbone architecture.

Dataset	Baselines		Benchmarks					Ours
	Mean	MF	CSDI	MDOT	PSW	BRITS	nMW	DRIO
<i>MSE (Imputation Accuracy)</i>								
CNNpred	1.11(0.14)	1.45(0.27)	0.80(0.05)	0.89(0.34)	1.06(0.20)	0.53(0.17)	2.58(3.17)	0.52(0.17)
PEMS08	1.27(0.46)	2.42(3.32)	14.11(11.97)	0.64(0.50)	0.28(0.15)	0.42(0.27)	3.31(3.81)	0.45(0.26)
PM2.5	1.53(0.33)	2.00(0.37)	1.10(0.35)	1.18(0.18)	0.22(0.20)	0.93(0.21)	3.10(2.43)	0.60(0.13)
GasSensor	1.09(0.23)	0.44(0.16)	0.56(0.40)	0.32(0.28)	0.01(0.02)	0.06(0.04)	2.07(3.26)	0.07(0.05)
Gait	0.30(0.03)	0.82(0.75)	0.04(0.06)	0.15(0.11)	0.22(0.35)	0.15(0.19)	2.80(3.63)	0.14(0.14)
PEMS04	0.95(0.06)	1.72(2.20)	3.66(5.81)	0.42(0.24)	0.40(0.12)	0.43(0.20)	3.13(3.83)	0.41(0.16)
CMAPSS	1.08(0.08)	1.08(0.16)	0.08(0.13)	0.69(0.23)	0.87(0.13)	0.29(0.30)	0.59(0.69)	0.22(0.21)
AirQuality	0.80(0.06)	1.77(1.75)	0.15(0.17)	0.46(0.34)	0.39(0.30)	0.25(0.20)	2.78(4.21)	0.24(0.17)
HAR	1.01(0.05)	1.68(0.18)	0.21(0.23)	0.64(0.19)	0.34(0.28)	0.34(0.35)	2.42(2.48)	0.23(0.25)
PhysioNet	1.03(0.04)	1.96(0.42)	0.48(0.16)	0.85(0.18)	0.62(0.12)	0.58(0.16)	7.85(9.87)	0.52(0.16)
<i>W2 (Distributional Alignment)</i>								
CNNpred	0.23(0.15)	0.14(0.09)	0.31(0.26)	0.19(0.13)	0.10(0.08)	0.25(0.25)	0.82(1.13)	0.18(0.18)
PEMS08	0.28(0.19)	0.46(0.67)	1.62(1.44)	0.20(0.15)	0.05(0.04)	0.27(0.29)	0.99(1.25)	0.24(0.25)
PM2.5	0.33(0.22)	0.31(0.21)	0.30(0.21)	0.30(0.20)	0.11(0.16)	0.31(0.23)	0.85(1.05)	0.28(0.21)
GasSensor	0.34(0.23)	0.13(0.11)	0.33(0.10)	0.20(0.20)	0.01(0.01)	0.06(0.06)	0.78(1.19)	0.06(0.07)
Gait	0.07(0.05)	0.14(0.18)	0.05(0.08)	0.05(0.04)	0.09(0.14)	0.10(0.13)	0.89(1.24)	0.09(0.10)
PEMS04	0.24(0.16)	0.33(0.50)	0.50(0.40)	0.17(0.15)	0.06(0.05)	0.19(0.20)	0.96(1.26)	0.17(0.17)
CMAPSS	0.37(0.22)	0.19(0.11)	0.06(0.10)	0.21(0.14)	0.16(0.13)	0.19(0.22)	0.36(0.46)	0.18(0.21)
AirQuality	0.21(0.16)	0.33(0.45)	0.11(0.17)	0.16(0.16)	0.06(0.06)	0.18(0.22)	0.87(1.34)	0.14(0.17)
HAR	0.40(0.34)	0.11(0.08)	0.10(0.14)	0.25(0.24)	0.09(0.10)	0.22(0.26)	0.75(1.01)	0.18(0.21)
PhysioNet	0.36(0.28)	0.20(0.17)	0.18(0.14)	0.32(0.29)	0.14(0.12)	0.25(0.24)	1.48(2.00)	0.22(0.20)

C.5.2 Other Details

For computational efficiency, we conduct this ablation study on four representative datasets: PEMS08 ($N=170$, $D=3$, $T=62$), Gait ($N=300$, $D=6$, $T=101$), C-MAPSS ($N=359$, $D=21$, $T=207$), and PhysioNet ($N=4000$, $D=35$, $T=48$), under MCAR and MNAR and missing ratios of 10%, 50%, and 90%. These datasets provide diverse coverage across sample sizes (170–4000), feature dimensions (3–35), and sequence lengths (48–207), ensuring the comparison generalizes across varying data characteristics.

For objective functions, we compare MSE, DRIO with balanced Sinkhorn (BSH-DRIO), and the original BRITS objective. BSH-DRIO uses balanced optimal transport with strict mass conservation (S_ε) instead of the unbalanced variant ($S_{\varepsilon,\tau}$) that relaxes marginal constraints via the parameter τ . The balanced formulation enforces $\pi_1 = \mu$ and $\pi_2 = \nu$ exactly, whereas our unbalanced formulation penalizes marginal deviations with KL divergence scaled by τ (See Appendix A for details). The original BRITS objective combines MSE reconstruction with a consistency loss that penalizes discrepancies between forward and backward RNN predictions, providing an alternative form of regularization without distributional robustness.

All models are trained with the Adam optimizer using learning rate 5×10^{-4} and weight decay 10^{-6} . We use batch size 32 and train for 30 epochs, evaluating on the validation set every 10 epochs. For the DRIO-based objective, we use 5 inner optimization steps with inner learning rate 0.01 for the adversarial weight update.

Table 6: Imputation results under MNAR missing mechanism. Values show mean(std) across 10%, 50%, and 90% missing ratios. Bold indicates top 3 per dataset. DRIO is paired with BRITS backbone.

Dataset	Baselines		Benchmarks					Ours
	Mean	MF	CSDI	MDOT	PSW	BRITS	nMW	DRIO
<i>MSE (Imputation Accuracy)</i>								
CNNpred	1.35(0.05)	1.67(0.06)	1.31(0.45)	0.98(0.35)	1.31(0.22)	0.76(0.23)	2.24(2.20)	0.74(0.21)
PEMS08	1.20(0.15)	2.37(2.76)	49.76(57.47)	0.65(0.36)	0.38(0.11)	0.54(0.23)	2.83(3.05)	0.52(0.15)
PM2.5	1.49(0.27)	1.76(0.35)	1.07(0.28)	1.17(0.37)	0.42(0.43)	0.91(0.46)	3.00(2.63)	0.63(0.44)
GasSensor	1.40(0.27)	0.57(0.31)	0.64(0.52)	0.41(0.35)	0.02(0.02)	0.08(0.07)	1.28(1.87)	0.09(0.06)
Gait	0.33(0.06)	0.85(0.79)	0.07(0.10)	0.18(0.16)	0.30(0.46)	0.21(0.28)	2.47(2.78)	0.15(0.16)
PEMS04	0.81(0.14)	1.55(1.79)	0.24(0.14)	0.41(0.19)	0.38(0.08)	0.43(0.14)	2.68(2.99)	0.41(0.12)
CMAPSS	1.15(0.03)	1.16(0.14)	0.14(0.23)	0.79(0.20)	0.93(0.10)	0.36(0.34)	0.65(0.61)	0.27(0.26)
AirQuality	0.92(0.08)	1.73(1.49)	0.21(0.27)	0.54(0.42)	0.41(0.33)	0.35(0.34)	2.34(3.42)	0.32(0.28)
HAR	1.23(0.18)	1.90(0.06)	0.29(0.28)	0.77(0.14)	0.42(0.29)	0.46(0.41)	2.16(1.49)	0.33(0.36)
PhysioNet	1.35(0.42)	2.26(0.35)	0.75(0.27)	1.13(0.29)	0.72(0.11)	0.87(0.26)	7.83(9.43)	0.79(0.26)
<i>W2 (Distributional Alignment)</i>								
CNNpred	0.33(0.23)	0.20(0.12)	0.40(0.31)	0.29(0.22)	0.19(0.16)	0.36(0.36)	0.71(0.87)	0.32(0.32)
PEMS08	0.31(0.21)	0.46(0.66)	2.53(1.92)	0.25(0.21)	0.09(0.08)	0.32(0.34)	0.89(1.13)	0.29(0.30)
PM2.5	0.46(0.35)	0.36(0.27)	0.41(0.36)	0.42(0.36)	0.23(0.33)	0.44(0.41)	0.83(0.98)	0.39(0.38)
GasSensor	0.44(0.29)	0.15(0.12)	0.35(0.28)	0.28(0.28)	0.02(0.03)	0.10(0.13)	0.57(0.86)	0.06(0.06)
Gait	0.12(0.10)	0.16(0.17)	0.08(0.13)	0.09(0.10)	0.15(0.24)	0.17(0.23)	0.80(1.05)	0.11(0.13)
PEMS04	0.28(0.21)	0.34(0.47)	0.18(0.22)	0.22(0.20)	0.10(0.09)	0.25(0.25)	0.89(1.13)	0.23(0.23)
CMAPSS	0.40(0.24)	0.22(0.14)	0.10(0.16)	0.28(0.22)	0.21(0.17)	0.24(0.28)	0.39(0.45)	0.21(0.25)
AirQuality	0.30(0.25)	0.28(0.29)	0.16(0.24)	0.25(0.27)	0.14(0.18)	0.27(0.33)	0.79(1.17)	0.21(0.28)
HAR	0.46(0.36)	0.13(0.07)	0.17(0.22)	0.33(0.30)	0.15(0.18)	0.32(0.36)	0.65(0.71)	0.26(0.32)
PhysioNet	0.45(0.27)	0.23(0.10)	0.26(0.14)	0.41(0.28)	0.21(0.15)	0.36(0.27)	1.47(1.93)	0.33(0.22)

C.6 Additional Results

C.6.1 MCAR Imputation Performance

Table 5 presents MSE and W2 under MCAR, with mean and standard deviation calculated across missing ratios. For MSE, DRIO is the only method to achieve top-3 performance across all 10 datasets, demonstrating its consistent imputation quality. DRIO attains the lowest MSE on CNNpred (0.52 ± 0.17) and remains competitive elsewhere, while exhibiting notably low variance compared to alternatives. Simple baselines (Mean, MF) consistently underperform with MSE often exceeding 1.0. CSDI achieves strong results on several datasets (Gait: 0.04 ± 0.06 , CMAPSS: 0.08 ± 0.13 , AirQuality: 0.15 ± 0.17) but can fail on traffic data with extremely high variance (PEMS08: 14.11 ± 11.97 , PEMS04: 3.66 ± 5.81), indicating that diffusion-based methods can be unstable with non-stationary temporal patterns. PSW achieves the lowest MSE on datasets with higher temporal dimension (PEMS08, PM2.5, GasSensor, PEMS04), though its performance varies considerably across datasets. Notably, notMIWAE (nMW) exhibits the highest variance across all datasets (e.g., PhysioNet: 7.85 ± 9.87), suggesting poor reliability without correct missingness mechanism specification.

For W2, we note that DRIO minimizes worst-case Sinkhorn divergence over an ambiguity set rather than sample Wasserstein distance. Therefore, it hedges against distribution shift at the cost of not always achieving minimum W2. That said, DRIO achieves top-3 performance on 7 of 10 datasets with consistent standard deviations (typically 0.17–0.25), indicating effective and stable alignment of the underlying distribution. As for other methods, PSW generally achieves the lowest W2 with remarkably low variance on GasSensor (0.01 ± 0.01), as expected since it directly optimizes

Table 7: Hyperparameter selection comparison: Our reconstruction-based CV vs Oracle (ground-truth missingness CV). Each cell shows Ours (α, γ) / Oracle (α, γ).

Dataset	Mechanism	Missing Ratio		
		10%	50%	90%
CNNpred	MCAR	(0.75, 5) / (0.99, 10)	(0.99, 10) / (0.99, 10)	(0.75, 10) / (0.75, 10)
	MNAR	(0.99, 10) / (0.75, 1)	(0.75, 5) / (0.75, 5)	(0.75, 5) / (0.99, 10)
PEMS08	MCAR	(0.99, 10) / (0.99, 10)	(0.99, 10) / (0.99, 1)	(0.99, 1) / (0.99, 10)
	MNAR	(0.99, 10) / (0.75, 5)	(0.99, 1) / (0.99, 5)	(0.99, 0.1) / (0.99, 10)
PM2.5	MCAR	(0.99, 10) / (0.75, 5)	(0.99, 10) / (0.99, 10)	(0.99, 10) / (0.99, 10)
	MNAR	(0.99, 0.1) / (0.99, 10)	(0.99, 10) / (0.99, 10)	(0.99, 10) / (0.99, 10)
GasSensor	MCAR	(0.99, 5) / (0.99, 1)	(0.99, 0.1) / (0.99, 0.1)	(0.99, 0.1) / (0.99, 1)
	MNAR	(0.99, 5) / (0.99, 5)	(0.99, 5) / (0.99, 5)	(0.99, 1) / (0.99, 1)
Gait	MCAR	(0.99, 0.1) / (0.99, 0.1)	(0.99, 5) / (0.99, 5)	(0.99, 10) / (0.5, 1)
	MNAR	(0.99, 0.1) / (0.99, 0.1)	(0.99, 5) / (0.99, 5)	(0.99, 5) / (0.75, 5)
PEMS04	MCAR	(0.99, 10) / (0.99, 10)	(0.99, 0.1) / (0.99, 10)	(0.99, 0.1) / (0.99, 0.1)
	MNAR	(0.99, 10) / (0.75, 5)	(0.99, 0.1) / (0.99, 1)	(0.99, 0.1) / (0.99, 0.1)
C-MAPSS	MCAR	(0.99, 0.1) / (0.99, 10)	(0.99, 0.1) / (0.99, 0.1)	(0.99, 0.1) / (0.5, 1)
	MNAR	(0.99, 10) / (0.99, 0.1)	(0.99, 10) / (0.99, 10)	(0.99, 1) / (0.99, 1)
AirQuality	MCAR	(0.99, 0.1) / (0.99, 0.1)	(0.99, 0.1) / (0.99, 0.1)	(0.99, 10) / (0.99, 10)
	MNAR	(0.99, 0.1) / (0.99, 0.1)	(0.99, 5) / (0.99, 0.1)	(0.99, 10) / (0.99, 10)
PhysioNet	MCAR	(0.75, 10) / (0.99, 5)	(0.99, 10) / (0.99, 10)	(0.99, 5) / (0.99, 10)
	MNAR	(0.99, 10) / (0.99, 0.1)	(0.99, 5) / (0.99, 10)	(0.99, 0.1) / (0.99, 0.1)

Wasserstein distance. The stability advantage of DRIO becomes particularly evident in the W2 metric, where methods like CSDI show high variance on traffic datasets (PEMS08: 1.62 ± 1.44) while DRIO maintains moderate and consistent values (PEMS08: 0.24 ± 0.25).

C.6.2 Variance Analysis under MNAR.

Table 6 reveals important stability characteristics under the more challenging MNAR mechanism. Compared to MCAR (Table 5), most methods exhibit increased variance under MNAR, reflecting the additional difficulty posed by systematic missingness. We found that CSDI’s failure on traffic data becomes even more severe, with PEMS08 showing MSE of 49.76 ± 57.47 , indicating complete instability when diffusion-based generation encounters value-dependent missingness in non-stationary data. Similarly, notMIWAE exhibits persistently high variance across all datasets (e.g., PhysioNet: 7.83 ± 9.43 for MSE, 1.47 ± 1.93 for W2), confirming that its performance is unreliable without accurate specification of the missingness mechanism.

In contrast, DRIO demonstrates robust stability under MNAR, with MSE standard deviations ranging from 0.12 to 0.44, which is substantially lower than competing deep learning methods. This stability advantage is particularly evident on datasets where other methods struggle. For W2, DRIO maintains consistent standard deviations (0.06–0.38) across datasets, whereas CSDI shows high variance on traffic data (PEMS08: 2.53 ± 1.92). PSW achieves the lowest variance on GasSensor (0.02 ± 0.02 for MSE, 0.02 ± 0.03 for W2) due to its direct Wasserstein optimization, though this stability does not transfer uniformly across all datasets. These results confirm that DRIO’s

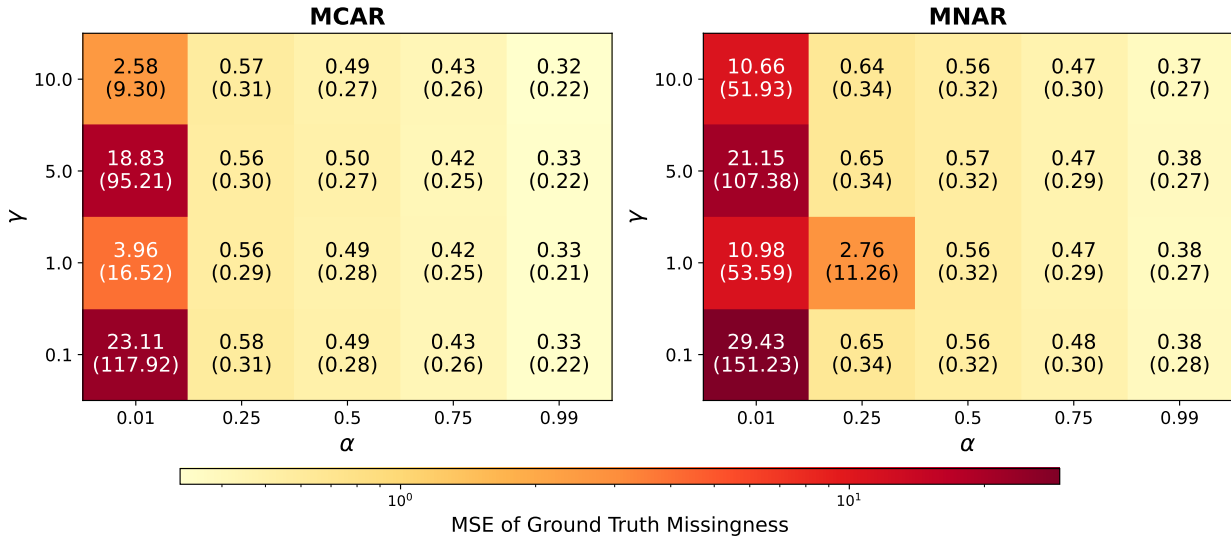


Figure 4: Validation MSE on artificial missing entries across the hyperparameter grid, averaged over all datasets. Values show mean \pm standard deviation. Lower is better.

distributionally robust regularization provides effective hedging against the compounded challenges of non-stationarity and systematic missingness, yielding both accurate and stable imputation performance. a

C.6.3 Hyperparameter Sensitivity Analysis.

We provide a detailed analysis of hyperparameter sensitivity and validates our reconstruction-based cross-validation procedure for selecting the robustness parameters α and γ . For both methods, hyperparameter grid is $\alpha \in \{0.01, 0.25, 0.5, 0.75, 0.99\}$ and $\gamma \in \{0.1, 1.0, 5.0, 10.0\}$. Due to computational challenges, we conduct the analysis based on all datasets without HAR.

Hyperparameter Selection Comparison

Table 7 compares the hyperparameters selected by our reconstruction-based cross-validation procedure against the oracle method that has access to the ground-truth missingness pattern in validation set. Specifically, our method selects hyperparameters by minimizing reconstruction error on observed entries in the validation set (after artificial masking), while the oracle evaluates imputation quality directly on the truly missing entries.

Our reconstruction-based CV achieves exact hyperparameter agreement with the oracle in 24 out of 54 settings (44.44%). Both methods predominantly select $\alpha = 0.99$ across most settings. However, under 90% missingness, the oracle can select lower α values (e.g., $\alpha = 0.5$ for Gait MCAR and C-MAPSS MCAR, $\alpha = 0.75$ for Gait MNAR), while our CV consistently selects $\alpha = 0.99$ in these cases. This suggests that under extreme missingness, the oracle benefits from increased robustness emphasis, a signal our reconstruction-based validation can partially capture since the observed entries in the validation set may not reflect the severity of the true missing data distribution shift. That said, since $\alpha = 0.99$ dominates most cases, it indicates that prioritizing reconstruction fidelity is generally beneficial across diverse datasets and missingness mechanisms. As for γ , the disagreements between the two CV approaches tend to occur within the same order of magnitude (e.g., $\gamma \in (5, 10)$),

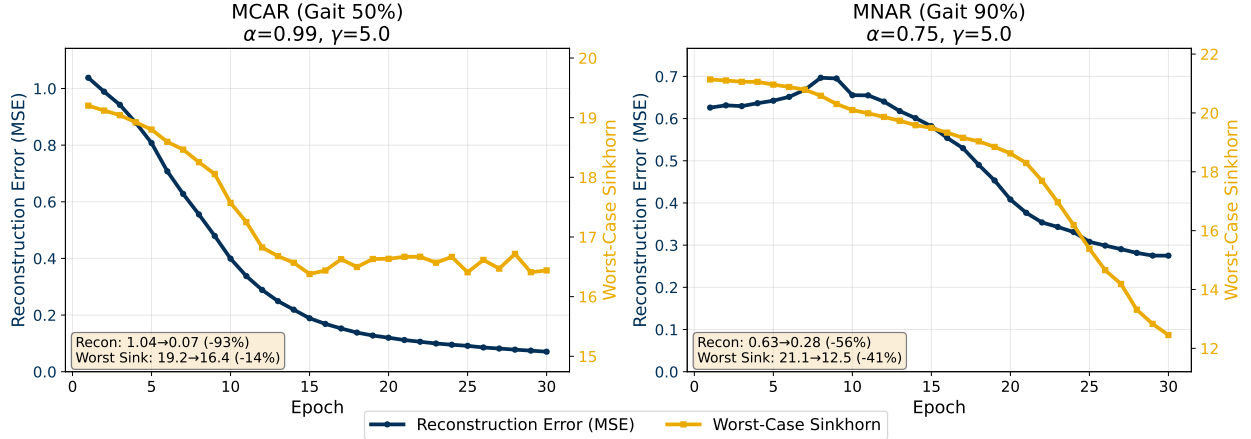


Figure 5: Training curves showing reconstruction error (MSE) and worst-case Sinkhorn divergence over epochs. Left: Gait MCAR 50% with $\alpha = 0.99$, $\gamma = 5.0$. Right: Gait MNAR 90% with $\alpha = 0.75$, $\gamma = 5.0$.

suggesting that the performance surface is relatively flat in these regions. This result is further confirmed by the sensitivity analysis next in Figure 4.

Hyperparameter Sensitivity

Figure 4 presents heatmaps of validation MSE (on the artificial missing entries), averaged over all nine datasets and missing ratios.

From Figure 4, we observe that for both MCAR and MNAR mechanisms, performance improves substantially as α increases from 0.01 to 0.99. At $\alpha = 0.01$, where the objective is dominated by the distributional robustness term, MSE values are an order of magnitude higher (e.g., 23.1 for MCAR, 29.4 for MNAR at $\gamma = 0.1$). This confirms that pure distributional matching without reconstruction guidance leads to poor imputation quality. In contrast, once $\alpha \geq 0.5$, performance becomes remarkably stable across different γ values. For MCAR, MSE ranges only from 0.32 to 0.49 across all (α, γ) combinations with $\alpha \geq 0.5$. Similarly for MNAR, MSE ranges from 0.37 to 0.65 in this region. This stability suggests that practitioners can achieve good results without extensive hyperparameter tuning by simply setting α to a high value (e.g., 0.99). We note that $\alpha = 0.99$ put MSE and the Sinkhorn Divergence roughly at the same scale, as presented next in the training curve Figure 5.

As for the Sinkhorn regularization strength γ , it has a less sensitive effect compared to α . At high α values, different γ settings yield similar performance, indicating that the distributional robustness term acts primarily as a regularizer rather than the dominant objective. The optimal γ tends to be higher (5.0 or 10.0) when α is also high, suggesting a complementary relationship between reconstruction emphasis and regularization strength, while α has a more direct influence on the validation error.

We note that the MNAR setting exhibits slightly higher sensitivity to hyperparameter choices, particularly at low α values. This is expected since MNAR missingness creates more challenging distributional shifts that require careful balancing between reconstruction and robustness objectives.

Training Dynamics

Figure 5 illustrates the training dynamics for two representative settings: Gait under MCAR with 50% missingness and MNAR with 90% missingness.

We note that both the reconstruction error and worst-case Sinkhorn divergence decrease during training, demonstrating that our bi-level optimization successfully minimizes both objectives. For MCAR 50%, reconstruction error decreases by 93% (from 1.04 to 0.07) while the Sinkhorn term decreases by 14% (from 19.2 to 16.4). For MNAR 90%, reconstruction error decreases by 56% (from 0.63 to 0.28) and the Sinkhorn term decreases by 41% (from 21.1 to 12.5).

Despite $\alpha = 0.99$ heavily weighting the reconstruction term in the objective, the actual magnitudes of the two loss components remain comparable during training. This is because the unbalanced Sinkhorn divergence operates on a different scale than MSE. Moreover, the hyperparameter γ effectively controls this balance, ensuring that the distributional robustness term provides meaningful regularization without overwhelming the reconstruction objective.